Subsidiary-absorption spin-wave-instability processes in yttrium iron garnet thin films: Coupled lateral standing modes, critical modes, and the kink effect

G. Wiese, P. Kabos, and C. E. Patton
Department of Physics, Colorado State University, Fort Collins, Colorado 80523
(Received 5 December 1994)

Subsidiary-absorption butterfly curves of the spin-wave-instability threshold microwave-field-amplitude versus static field H, for an in-plane magnetized 1.1 mm $\times$2.0 mm, 7-μm-thick yttrium iron garnet film rectangle at 9.4 GHz, and with the linearly polarized microwave field perpendicular to the static field H and also in-plane, are found to show significant changes when H is changed from along the long edge to along the short edge of the rectangle. This effect is explained by a theory for the first-order spin-wave-instability threshold in magnetic films, which takes into acocunt the coupled standing spin-wave modes across the lateral dimensions of the film. This theory is a modification of a previous theory, which considered the standing modes across the film cross section only. The theory is able to reproduce the orientation effect found experimentally and give good fits to the butterfly-curve data. In contrast with previous results, it is not necessary to introduce *ad hoc* spin-wave angle θ_K terms into the spin-wave linewidth to obtain these fits. The theory also yields critical-mode wave numbers in the kink region which are in the 5×10^4 cm^{-1} range, which agree with previous fine-structure and Brillouin light-scattering measurements. A key parameter in the analysis is a mode spacing parameter $\Delta\omega_K$, which contains a factor of the form $\sin(2\theta_K)/K$, where K is the mode wave number and θ_K is the mode in-plane angle relative to H. These dependences are the key to the match with experiment. They are also general, and not limited to the thin-film geometry.

I. INTRODUCTION

Ferromagnetic resonance (FMR) experiments in ferrite materials at high microwave power levels can lead to a number of nonlinear effects.[1,2] One of these effects, usually termed "subsidiary absorption," involves the parametric excitation of spin waves at one-half the pump frequency and a broad absorption region somewhat below the ferromagnetic resonance field.[3] At a given static magnetic field H, one finds a critical microwave-field amplitude for the onset of the absorption, usually called $h_{\rm crit}$. Plots of $h_{\rm crit}$ as a function of H over the static field range for subsidiary absorption, termed "butterfly curves," are generally used to study quantitatively the parametric spin-wave-instability processes which lead to the observed losses. The term "butterfly curve" was initially coined because of the characteristic sharp cusp evidenced by plots of $h_{\rm crit}$ vs H which was found for a second low-field absorption region which was found for narrow linewidth single-crystal yttrium iron garnet (YIG) spheres when the microwave field was applied in the same direction as the static field, a process termed "parallel pumping."[4] Spin-wave-instability processes and butterfly curves for subsidiary absorption and parallel pumping are reviewed by Patton.[5]

Subsidiary-absorption butterfly curves for single-crystal YIG spheres do not show sharp cusps. Rather, such curves show a rather complicated behavior,[6] with (a) a low static field region in which $h_{\rm crit}$ decreases slowly with increasing H, (b) a kink point at which $h_{\rm crit}$ decreases sharply, and (c) a range of fields corresponding to a broad subsidiary absorption peak for which $h_{\rm crit}$ is relatively small and may show considerable structure, depending on the geometry. Patton and Jantz[6] found that the kink occurs close to the point in static field at which the top of the spin-wave band at low wave number is at one-half the pump frequency. The kink was explained on the basis of existing first-order spin-wave-instability theory for bulk materials[7,8] and a wave-vector-dependent relaxation rate which promotes a jump of the critical mode from high wave numbers to zero wave number at a critical value of the static field. This jump produces a "kink" in the butterfly curve at that point. The wave-vector dependence which best reproduced the kink effect and gave a best fit to the data was found empirically but could be qualitatively justified on the basis of theory. Except for the region of low $h_{\rm crit}$, the spin-wave model yielded calculated butterfly curves which matched the data extremely well. In this low $h_{\rm crit}$ region, the measured $h_{\rm crit}$ values were somewhat below the calculated curves and the structure was indicative of parametrically excited magnetostatic modes at one-half the pump frequency. These results were recently reviewed by Chen and Patton.[9]

The butterfly-curve experiments cited above involved microwave measurements only. Wilber and co-workers[10] were able to verify directly the predicted field dependences for the critical spin-wave mode propagation angle relative to the static field which accompanied the kink effect by Brillouin light-scattering (BLS) measurements on in-plane magnetized YIG films. These measured propagation angles for the critical spin-wave modes were the same as predicted from the spin-wave theory. It was also possible by means of the BLS experiments to measure the wave numbers for the critical modes in the low

 ©1995 The American Physical Society

h_{crit} field regime. These measured critical-mode wave numbers were in the 10^4 cm^{-1} range, compared to the zero values predicted from the bulk-wave theory. For the mm–cm size YIG films used for the experiments, the low-order standing-wave magnetostatic modes for the film would have much lower wave numbers, in the 10–100 cm^{-1} range. Critical-mode wave numbers in the 10^4 cm^{-1} range are consistent with the subsidiary absorption fine-structure measurements of Jantz and Schneider for YIG spheres.[11]

Following these initial studies of spin-wave instability in YIG films, Wiese and co-workers were able to provide both a theoretical analysis of the instability processes[11] and a detailed experimental study[12] of the associated critical modes and butterfly curves for subsidiary absorption in films magnetized both in-plane and perpendicular to the film plane. The basic result is that spin-wave modes with an out-of-plane wave-vector component will have a higher threshold. Where allowed, therefore, the modes with the lowest threshold will tend to have their wave vectors in plane. For the in-plane field case, one can keep the wave vector in plane and still have the full range of propagation angles relative to the static field, so that one can obtain the same kink effect as for spheres. This explained the successful observation of the kink effect for in-plane magnetized films in the earlier BLS experiments of Wilber *et al.*[10] The in-plane field data matched the previous microwave measurements; the theory gave a good fit to the data and supported the basic kink effect results of the earlier workers.

In the perpendicular magnetized film case, however, the spin-wave wave vector will have an out-of-plane component for all propagation angles except 90°. This leads to additional constraints on the critical modes for the thin-film geometry which serve to eliminate the kink effect. For the perpendicular field case, the measurements showed a perfectly smooth, almost featureless, butterfly curve with no kinks or extra structure of any kind. The theory matched the data nicely.

While the BLS results of Wilber *et al.* provided a direct verification of the subsidiary-absorption critical-mode properties predicted from bulk theory and the work of Wiese and co-workers demonstrated the effect of the thin-film geometry on the critical modes, two problems remain: (1) the origin of the **k**-dependent spin-wave relaxation rate, or equivalently, the spin-wave linewidth, which played a crucial role in the model; and (2) the origin of the much larger than expected wave numbers for the critical modes in the low h_{crit} field regime for the in-plane magnetized films.

The present work provides an additional perspective on subsidiary absorption for single-crystal YIG materials in general and thin films in particular. The experiments utilized an in-plane magnetized 7-μm-thick rectangular 2.0×1.0 mm single-crystal YIG film, with a 10-GHz linearly polarized microwave pump field in plane and perpendicular to the static field. The new experimental result is that the shape of the butterfly curve in the low h_{crit} regime for static fields above the kink point depends on the orientation of the film relative to the static field. The low h_{crit} field regime extends to slightly smaller static field values, by about 50 Oe, and has a shallower minimum, by about 15%, when the long edge of the film is parallel to the static field then when the field and the short edge are parallel. This result clearly demonstrates that the standing waves across the lateral film dimensions play an important role in the subsidiary-absorption process for films.

In addition to this basic experimental result, application of the theory in Ref. 12 to the problem has led to a new understanding of the previous empirical results of Patton and Jantz concerning the **k**-dependent spin-wave linewidth and Wilber *et al.* concerning critical modes with wave numbers in the 10^4 cm^{-1} range. It was possible to apply the theory to the present problem by formally treating the lateral standing waves across the lateral dimensions of the film in the same way as the standing waves across the film thickness were treated in Refs. 12 and 13. This led to a coupled mode problem which was solved numerically to yield a simple result.

It was found that for a given set of coupled modes centered at some nominal wave vector K and frequency $\omega_K = \omega_p/2$, where ω_p is the pump frequency, the threshold has a simple form. The ratio of the instability threshold for the film, h_c^{film}, to the same threshold for a bulk sample, h_c^{bulk}, to a very good approximation, is a simple increasing function of a frequency shift parameter divided by the relaxation rate. The frequency shift parameter $\Delta\omega_K$ is related to the frequency separation for the lateral standing modes across the film, and depends on the value of the nominal spin-wave wave vector **K** at one-half the pump frequency and the film dimensions.

For a given static field, one obtains the actual h_{crit} and the corresponding critical mode in the usual way by finding the mode at one-half the pump frequency with the minimum value of h_c. This procedure yields butterfly curves which match the data nicely and reproduce the experimental changes with film orientation described above. The model, moreover, requires a spin-wave linewidth precisely of the form obtained by Sparks[14] from theoretical three-magnon scattering considerations. No special propagation angle-dependent term of the sort introduced in previous work on empirical grounds was needed. The model, furthermore, gives a critical-mode wave number of about 5×10^4 cm^{-1} in the low h_{crit} field regime, the range expected from the previous BLS results. This relatively high wave number range is derived from an inverse K dependence, where K denotes the nominal spin-wave wave number, for the $\Delta\omega_K$ function indicated above. This dependence comes solely from the form of the spin-wave dispersion for modes propagating in plane.

It appears, therefore, that coupled, lateral standing-mode spin waves can be used in combination with the thin-film instability theory of Ref. 12 to account for all of the presently known characteristics of subsidiary-absorption instability processes in YIG films. This general result carries over to other sample shapes as well. Even though the details of the standing modes are different, as in the case of the Walker modes for sphere-shaped samples, for example, the overall coupled mode problem is the same. This means that a proper, *albeit* complicated, coupled mode solution for any general sam-

ple shape should yield critical modes of the sort deduced empirically for sphere samples by Jantz and Schneider, Patton and Jantz, and Wilber *et al.*

The above change from a lower case k notation to a capital K notation is significant. In the usual bulk theory, one considers only single modes at one-half the pump frequency and some wave vector **k**. For coupled modes, this single mode is replaced by an array of coupled modes clustered around this single-mode point. One then uses **K** to denote the nominal wave vector at the array center and at a frequency $\omega_K = \omega_p/2$, and further uses an indexed sequence of lower case **k** parameters to denote the wave vectors for various coupled modes in the array. The corresponding wave numbers are K and k. These important notational considerations for the coupled mode analysis will be discussed in more detail below.

II. EXPERIMENT AND RESULTS

The subsidiary-absorption data were obtained on a (111) plane, 7-μm-thick YIG film at 9.4 GHz and room temperature. The film was in the shape of a rectangle with side lengths of 1.1 and 2.0 mm. The film was grown by conventional liquid phase epitaxy (LPE) techniques on gadolinium gallium garnet substrates and had a narrow ferromagnetic resonance half-power linewidth of about 0.5 Oe at 10 GHz. The experimental setup for the measurements was the same as in Ref. 13. The butterfly-curve data were obtained with a modified Varian 4500 EPR spectrometer. A TWT amplifier was added to the microwave system to obtain the necessary cw power levels to measure complete butterfly curves. All measurements were made at room temperature. The adjustable iris TE102 reflection cavity was the same as used in Ref. 13. Only the sample and sample orientation were different. The change in loading shifted the frequency from the 9.3-GHz value in Ref. 13 to 9.4 GHz. The other cavity parameters were about the same as in Ref. 13, with a loaded Q of 3100 and a reflection coefficient of -9.54 dB at cavity resonance. Based on these parameters, the microwave field power response calibration constant for the cavity, based on the empty cavity mode configuration, was 5.625 Oe^2/W.

The YIG film was mounted on a sample holder which allowed for rotation of the rectangular sample between two configurations, a "long" configuration and a "short" configuration. In the long configuration, the applied in-plane static magnetic field H was parallel to the longer 2.0-mm edge of the rectangular film. In the short configuration, the field H was parallel to the shorter 1.1-mm edge of the film. The linearly polarized microwave pump field was always in plane and perpendicular to the static field. Butterfly curves of the instability threshold microwave field amplitude h_{crit} as a function of the static field H were obtained with the technique of Patton and Jantz.[6] In this technique, the static field is swept at constant microwave power and the field point for the abrupt increase in absorption which marks the instability threshold is measured. This procedure is then repeated for a large number of power levels, and the calibrated data are to construct butterfly curves.

Typical butterfly curves for the long and the short configurations are shown in Fig. 1. The graphs show values of the threshold microwave field amplitude h_{crit} vs the static magnetic field H for the long and the short configurations as indicated. Both sets of data show the expected kink, which is close to $H=1100$ Oe for the long configuration and close to $H=1150$ Oe for the short configuration. The region of low h_{crit} for both butterfly curves extends from about 1200 Oe up to 1700 Oe. Above $H=1700$ Oe, the h_{crit} for both curves increases rapidly to the usual first-order spin-wave-instability cutoff for spin waves at one-half the pump frequency.

As outlined in the Introduction, one can understand the kink effect by analyzing these butterfly-curve data within the usual spin-wave approximation and with a wave-vector-dependent spin-wave linewidth.[6,10,13] One obtains critical modes on the low-field side of the kink with a propagation angle θ_k relative to the static field direction in the 30°–40° range and a nominal wave number k in the $3-4\times10^5$ cm^{-1} range. For fields above the kink point, the critical modes jump to $k\approx0$. The critical mode θ_k value starts out at about 80° just above the kink and decreases smoothly to zero at the high-field half-frequency cutoff point. The kink itself corresponds to a jump of the critical-mode wave vector from high to low k values and has its origin in the k dependence of the spin-wave relaxation rate which promotes instability for low k modes.

The new result in Fig. 1, however, is in the difference between the low h_{crit} portions of the butterfly curves for the long and the short configurations. Within the spin-wave approximation, one would expect *no difference* between these configurations. It is clear from the data, however, that the direction of the static field relative to the two edges of the rectangular sample does have a definite effect on the butterfly curve in the field region

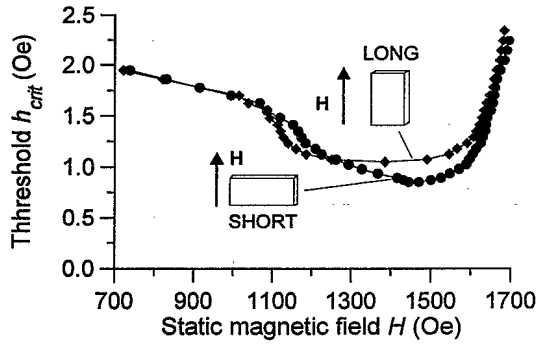

FIG. 1. Experimental subsidiary absorption butterfly curves of the spin-wave-instability threshold microwave field amplitude h_{crit} as a function of the in-plane static external magnetic field H for a 2.0 mm by 1.1 mm rectangular shaped 7-μm-thick single-crystal yttrium iron garnet film and a linearly polarized microwave pump field at 9.4 GHz. The circle data points are for the "long" case, with the field parallel to the long 2.0-mm edge of the sample. The diamond data points are for the "short" case, with the field parallel to the short 1.1-mm edge of the sample.

above the kink. In this region, the two butterfly curves show a crossover at about 1250 Oe. For static fields below the crossover point, the h_{crit} values for the short configuration are larger. For fields above crossover, the h_{crit} values for the long configuration are larger. It is noteworthy that the critical mode θ_k value for half-frequency spin waves at this crossover point is close to 45°. This will be an especially important point of consideration for the theoretical results to follow.

It will be evident from the analysis given below that the effect of sample shape is both subtle and general, and is ultimately derived from the coupling between the various standing-wave normal modes of the sample at frequencies close to one-half the microwave pump frequency. This coupling includes, among other things, a factor in the frequency shift parameter $\Delta\omega_K(\mathbf{K})$ which has the form $\sin(2\theta_K)/K$. The $\sin(2\theta_K)$ term has the same effect on the critical-mode selection process which was served by the *ad hoc* $\sin^2(2\theta_k)$ spin-wave linewidth term in the fits by Patton and Jantz. The $1/K$ term promotes a critical-mode preference for moderate K values in the 10^4 cm^{-1} range, rather than critical-mode wave numbers near zero.

Moreover, while the details of the numerical calculations given below are specifically for the standing-wave normal modes of a thin film, the critical $\sin(2\theta_K)/K$ factor in the analysis is independent of the actual shape of the sample. This means that the basic result is of general validity and applicable to other sample shapes as well. In particular, the results should be applicable to the YIG sphere data of Jantz and Schneider and Patton and Jantz. The coupled mode model, therefore, appears to resolve the two remaining problems in subsidiary absorption noted above, not only for thin films, but also for sphere-shaped samples and other shapes as well.

III. THEORY

As indicated above, the origin of the differences in the butterfly curves in Fig. 1 lies in the details of the coupling between the various lateral standing spin-wave modes for the rectangular film. The first-order spin-wave-instability theory for the discrete standing spin waves across the film cross section is discussed in detail in Ref. 12. The key elements of this theory are also summarized in Ref. 13. The present problem concerns the case of in-plane magnetized films only. As discussed in Ref. 13 and also indicated above, for this case one need only consider spin waves with the wave-vector $\mathbf{k}$ in plane and with a uniform dynamic response across the film cross section. When $\mathbf{k}$ is in plane, the film edges set up constraints on the allowed $\mathbf{k}$ values which lead to standing-wave modes with an integral number of half wavelengths between parallel sides for a rectangular sample. These are the lateral standing modes which are considered here. The material below summarizes basic physical considerations and operational equations from the theory of Refs. 12 and 13, with appropriate modifications to deal with the lateral standing modes. Specific numerical results and connections with the experimental results of Sec. II are presented in Sec. IV.

The model ignores the possibility of nonzero values for the $\mathbf{k}$ component perpendicular to the film. In LPE YIG films, there are often interface effects which serve to limit the dynamic response at the film surfaces. These effects, termed "pinning," can force the perpendicular $\mathbf{k}$ component to be nonzero. Such effects for the present films were found to be small. Ferromagnetic resonance (FMR) spectra for the in-plane static field case had a large uniform mode FMR signal and much smaller signals for the sequence of peaks usually associated with spin-wave resonance and pinning. For the 7-μm-thick films used here, moreover, typical values for the perpendicular component of $\mathbf{k}$ in pinned films are in the 5×10^3 cm^{-1} range. The results below indicate critical mode $|\mathbf{k}|$ of $0.5-1.0\times10^5$ cm^{-1} or greater, a factor of 10 or more larger than such perpendicular components.

The geometry of the problem is shown in Fig. 2. The diagram in Fig. 2(a) shows the spin-wave wave vector configuration. The magnetic sample is magnetized to saturation in the z direction. The static magnetic field $\mathbf{H}$ and the saturation magnetization $\mathbf{M}_s$ lie along the z axis. The spin-wave wave vector $\mathbf{k}$ is specified by the wave number k and the usual polar and azimuthal angles, θ_k and ϕ_k, respectively. It is important to keep in mind that the spin-wave modes considered in the subsidiary absorption theory of Refs. 12 and 13 for thin films are standing modes. Such modes are composed of the superposition of two modes with wave vectors of $+\mathbf{k}$ and $-\mathbf{k}$. Figure 2(a) shows only the wave vector $\mathbf{k}$ for one of the propagating modes which make up the standing mode. As in Ref. 13, the frequencies of the coupled modes will be close to one-half the pump frequency, or $\omega_p/2$. A crucial consideration for subsidiary absorption is in the values of θ_k and ϕ_k for the strongest coupling. For the problem at hand, the modes with the strongest coupling are taken to have $\mathbf{k}$ in plane, such that ϕ_k is 90°. This is the basic re-

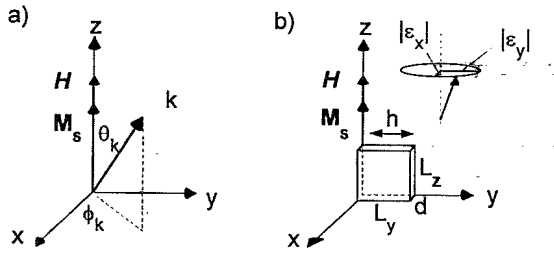

FIG. 2. Coordinate x-y-z representations for the field, magnetization, and spin-wave propagation directions, sample orientation, and microwave pumping configuration: (a) coordinate system for the static magnetic field $\mathbf{H}$, static magnetization $\mathbf{M}_s$, spin-wave wave vector $\mathbf{k}$, and spin-wave propagation angles θ_k and ϕ_k; (b) coordinate system for the sample, with the rectangular film of lateral dimensions L_y and L_z and thickness d in the y-z plane, $\mathbf{H}$ and $\mathbf{M}_s$ in the z direction, and the linearly polarized microwave field $\mathbf{h}$ in the y direction. In (b), a schematic elliptical precession cone diagram for the uniform precession mode is also shown. In this diagram, $|\epsilon_x|$ and $|\epsilon_y|$ denote the relative amplitudes of the x and y components of the uniform precession microwave magnetization response.

sult of the work in Ref. 13, also confirmed by Brillouin light-scattering measurements.[10] The specific analysis developed below will be for this special case only.

The connections with the experimental field and pumping configurations are shown in Fig. 2(b). The z-directed static field and magnetization vectors are both in plane. The diagram shows a rectangular film sample of thickness d and with lateral dimensions L_y and L_z. The linearly polarized microwave pump field $\mathbf{h}$ is in the y direction, also in plane. The in-plane microwave field yields an elliptically polarized uniform precession mode for the magnetization, as indicated by the x-y precession cone ellipse in Fig. 2(b). The relative lengths of the principal ellipse axes are denoted in terms of ellipticity factors ϵ_x and ϵ_y. These factors will be important in the analysis given below. Note that the geometry here is slightly different from the in-plane static field "IP" case of Ref. 13. There, the microwave field was out of plane.

The starting point for the formal theory is with the coupled equations of motion for the various spin-wave amplitudes which participate in the subsidiary absorption instability. One considers the set of standing spin-wave amplitudes b_k which are parametrically pumped by a linearly polarized microwave magnetic field of frequency ω_p applied perpendicular to the static field and saturation magnetization direction. The parametric excitation of the standing spin-wave modes at frequencies close to one-half the pump frequency can be described by an equation of the form[13]

$$\dot{b}_k(t)=-\left[\eta_k+i\left[\omega_k-\frac{\omega_p}{2}\right]\right]b_k(t)+\sum_{k'}C_{kk'}hb_{k'}^*(t)\ , \quad (1)$$

where $b_k(t)$ denote the complex time-dependent amplitudes of the standing spin waves, η_k is a relaxation rate, and ω_k is the frequency of the b_k mode. The $C_{kk'}$ coefficient describes the coupling between b_k and $b_{k'}$ amplitudes induced by the linearly polarized microwave pump field at frequency ω_p and of some complex amplitude h which takes the phase of the pump signal into account. It is important to emphasize that Eq. (1) applies to mode amplitudes for standing modes. The $b_k(t)$ represent mode amplitudes. The harmonic time dependences for b_k, at frequency ω_k, and for h, at frequency ω_p, have already been factored out of the equation. The b_k also correspond to standing modes composed of the superposition of *two* modes with wave vectors of $+\mathbf{k}$ and $-\mathbf{k}$. The k and k' subscripts in Eq. (1) and the other equations to follow are intended to denote these standing-wave $\mathbf{k}$ modes. A detailed, if somewhat compact, rendition of the complete formal theory is contained in Ref. 12.

The relaxation rate η_k is often specified in linewidth units by means of a spin-wave linewidth parameter $\Delta H_k=2\eta_k/\gamma$, where γ is the gyromagnetic ratio for the material, taken as positive. For YIG, γ is taken as 1.76×10^7 rad/Oe s, or 2.8 GHz/kOe, the same as for free electrons. It is important to realize that the relaxation parameters η_k and ΔH_k are $\mathbf{k}$ dependent. The use of suitable trial functions for $\Delta H_k(\mathbf{k})$ were crucial to the theoretical butterfly curve fits in Refs. 6 and 13. In this work, as will be shown later, only the $\Delta H(\mathbf{k})$ which is strictly appropriate to three-magnon scattering will be needed to obtain butterfly curves which match the data. The spin-wave linewidth will be considered in more detail shortly.

The coupled parametric mode problem defined in Eq. (1) can be approached in different ways. In Sec. III A, the bulk limit is considered. The theory in this limit is equivalent to the spin-wave-instability theory formulations by Suhl and Schlömann cited above. This limit was the basis for the various fits and conclusions concerning critical-mode kink effects and spin-wave linewidth $\mathbf{k}$ dependences by Patton and Jantz and Wilber *et al.* The discussion of this limit will serve to introduce the basic elements of the theory and establish basic formulas which will also be needed for the lateral mode theory of Sec. III B. The lateral mode theory will consider the explicit effect on the subsidiary-absorption threshold of the various standing modes across the film, in much the same way that the theory in Ref. 12 considered the effect of the standing modes across the film cross section. For the purposes of this analysis, the spin-wave wave vectors will be taken to be in plane, with the component of the wave vector perpendicular to the film plane set to zero. Most of the discussion in Sec. III B will concern the procedure for setting up the coupled mode eigenvalue problem to determine the effect of the coupling on the thresholds, based on the relevant terms in the set of coupled equations implicit in Eq. (1). Section III C will consider specific aspects of the eigenvalue problem which lead to a simple operational equation for the instability threshold microwave field amplitude for a given cluster of spin-wave states centered at one-half the pump frequency.

A. The bulk limit theory

In the case of very large or "bulk" samples, adjacent modes will be very close in frequency. In this limit, then, the coupled modes may be taken as a single mode at $\omega_k=\omega_p/2$ and $\mathbf{k}$. The matrix of $C_{kk'}$ coefficients is then taken as diagonal, according to $C_{kk'}=C_{kk}^{\text{bulk}}\delta_{kk'}$. One then seeks amplitude solutions of the form $b_k(t)=b_k e^{\beta t}$, where the exponential growth parameter β defines the threshold. The value of $|h|$ for which β is just zero corresponds to the spin-wave-instability threshold microwave field amplitude h_c^{bulk} for the particular spin-wave wave vector $\mathbf{k}$ and standing spin-wave amplitude b_k. In this diagonal limit, substitution of $b_k(t)=b_k e^{\beta t}$ and $C_{kk'}=C_{kk}^{\text{bulk}}\delta_{kk'}$ in Eq. (1) leads immediately to the condition $\beta=-\eta_k+|C_{kk}^{\text{bulk}}||h|$. The threshold h_c^{bulk} is just the value of $|h|$ required to satisfy $\beta=0$, given as $h_c^{\text{bulk}}=\eta_k/|C_{kk}^{\text{bulk}}|$. It is important to note that these threshold expressions involve only the absolute values of h and C_{kk}^{bulk}. The various phase factors which enter into the details of the dynamic response play no role in the final result.

A general expression for C_{kk}^{bulk} applicable to films is given in Ref. 13. For the present problem, with $\mathbf{k}$ in plane and ϕ_k at 90°, C_{kk}^{bulk} may be written as

$$C_{kk}^{\text{bulk}}=\frac{\gamma\omega_m}{4\epsilon_k}\sin\theta_k\cos\theta_k(\epsilon_y+\epsilon_x\epsilon_k)\ . \tag{2}$$

In Eq. (2), $\omega_m=\gamma 4\pi M_s$ denotes the saturation induction $4\pi M_s$ in frequency units, the ϵ_x and ϵ_y are uniform mode ellipticity factors introduced above, and ϵ_k is a spin-wave ellipticity factor. The ϵ_x and ϵ_y parameters are defined in terms of the uniform mode dynamic magnetization response $\mathbf{m}(t)$ to the transverse microwave pump field. For the pump configuration in Fig. 2(b) and a specific linearly polarized pump field of the form $h_y=he^{-i\omega_p t}$, one may write $\mathbf{m}(t)$ in the form

$$\mathbf{m}(t)=\frac{\gamma M_s h}{2}(\epsilon_x\mathbf{x}+i\epsilon_y\mathbf{y})e^{-i\omega_p t}\ , \tag{3}$$

where $\mathbf{x}$ and $\mathbf{y}$ denote unit vectors in the x and y directions, respectively. The ϵ_x and ϵ_y parameters defined through Eq. (3) are given by

$$\epsilon_x=i\left[\frac{1}{\omega_p-\omega_0}+\frac{1}{\omega_p+\omega_0}\right] \tag{4}$$

and

$$\epsilon_y=i\frac{\omega_0}{\omega_H}\left[\frac{1}{\omega_p-\omega_0}-\frac{1}{\omega_p+\omega_0}\right]\ , \tag{5}$$

where $\omega_H=\gamma H$ is the usual Zeeman frequency and $\omega_0=[\omega_H(\omega_H+\omega_m)]^{1/2}$ is the uniform mode ferromagnetic resonance frequency for the in-plane magnetized film. The expressions in Eqs. (4) and (5) differ from the corresponding expressions in Ref. 12 by a factor of -1. This is due to an additional common phase factor in the response formulas of Ref. 12. Such common phase factors, as already indicated, will not affect threshold field results.

Turn now to the properties of the spin waves. The spin-wave ellipticity parameter ϵ_k in Eq. (2) relates to the shape of the spin-wave precession cone in the limit of $k\gg 1/d$, where d is the film thickness. This parameter is given by[12,13]

$$\epsilon_k=\frac{\omega_k}{[\gamma(H+Dk^2)]}\ , \tag{6}$$

where D is the material spin-wave stiffness constant, typically 5.4×10^{-9} Oe cm^2 for YIG. Recall that the spin-wave modes of interest here, for the bulk limit, have frequencies at $\omega_k=\omega_p/2$. This condition, in combination with the spin-wave dispersion relation,

$$\omega_k=\gamma[(H+Dk^2)(H+Dk^2+4\pi M_s\sin^2\theta_k)]^{1/2}\ , \tag{7}$$

yields a specific and simple connection between the wave number k and the angle θ_k. This means that the ellipticity factor can be viewed as a θ_k-dependent function $\epsilon_k(\theta_k)$. Note that the condition $\epsilon_k(\theta_k)\geq 1$ is always satisfied. For the thin-film coupled mode problem considered below, the modes will still be taken to have frequencies close to $\omega_k=\omega_p/2$ and a $k-\theta_k$ connection defined by this frequency condition and the dispersion equation in Eq. (7).

In addition to the above, actual butterfly-curve calculations also require an operational equation for the $\mathbf{k}$-dependent spin-wave linewidth. The previous works, cited above, have used a $\Delta H_k(\mathbf{k})$ of the form

$$\Delta H_k(\mathbf{k})=A_0+A_1\sin^2(2\theta_k)+B_1L(k/k_c)\ , \tag{8}$$

where A_0, A_1, B_1, and k_c are taken as fitting parameters and the $L(k/k_c)$ function describes the k-dependent relaxation rate for three-magnon confluence processes in YIG due to Sparks:[14]

$$L(x)=\frac{1}{1.39x}\ln\left[1+\frac{8x^2(1+2x^2)}{1+8x^2}\right]\ . \tag{9}$$

The physical basis for such a $\Delta H_k(\mathbf{k})$ function is discussed in detail by Patton and Jantz. Specific theoretical fits for subsidiary absorption in YIG films are further discussed in Ref. 13. The constant A_0 term represents all $\mathbf{k}$-independent relaxation processes which contribute to the spin-wave relaxation. The $A_1\sin^2(2\theta_k)$ term is an empirical term which was found by Patton and Jantz to yield a good fit to the extreme high-field region of the subsidiary absorption butterfly curve for YIG spheres at 10 GHz. While there is no sound theoretical basis for an additive term of this sort, Sparks[14] did obtain a $\sin^2(2\theta_k)$ factor in the spin-wave relaxation rate in certain limiting cases for three-magnon confluence relaxation. The $B_1L(k/k_c)$ term in Eq. (8), with the L function given in Eq. (9), represents the specific k-dependent relaxation obtained by Sparks[14] for the three-magnon confluence relaxation in YIG.

Based on the above working equations, one can calculate bulk limit subsidiary absorption butterfly curves for in-plane magnetized films for comparison with measured values of the h_{crit} threshold as a function of the static field H. The details of such calculations are given in Refs. 6, 9, and 13. As shown in Ref. 13, one can obtain satisfactory fits to thin-film data for reasonable values of the spin-wave linewidth fitting parameters. There are, however, two problems with these fits to the bulk limit theory, (i) the lack of any rigorous justification for the $A_1\sin^2(2\theta_k)$ term in the $\Delta H_k(\mathbf{k})$ function and (ii) the discrepancy between the $k=0$ prediction for the critical modes in the low h_{crit} region of the butterfly curve and the much higher values of the critical-mode wave numbers which are found experimentally. An additional problem, evident from the new experimental data in Fig. 1, is in the effect of the in-plane field orientation on the shape of the low h_{crit} region of the butterfly curve. The bulk limit theory applies to a film of infinite extent and cannot be used to address these differences.

B. Coupled lateral mode theory for thin films

It is possible to introduce a relatively simple modification to the formal theory for thin films given in Refs. 12 and 13 to take into account the lateral film dimensions. This procedure is described below. When this is done, and the coupling between the lateral standing modes across the film is taken into account, it is possible

to compute explicit butterfly curves for the long and short configurations depicted in Fig. 1 which show the same basic effects evident from the data.

The starting point for this coupled lateral mode theory is with the $C_{kk'}$ coupling coefficient in Eq. (1). General $C_{kk'}$ expressions for in-plane and perpendicular-to-plane magnetized films of infinite extent are given in Refs. 12 and 13. The physical connection of importance here has to do with the effect of the thin film geometry on $C_{kk'}$ when the standing-mode spin-wave wave vector is perpendicular to the film. As discussed in Refs. 12 and 13, the change from the bulk limit is twofold. First, the nonvanishing $C_{kk'}$ coefficients are no longer the diagonal terms for which k and k' are equal, but rather, become the elements for which k' and k differ by some integral multiple of π/d. This selection rule relates to the usual standing modes across the film cross section, with k values of $n\pi/d$, where n is an integer. Second, these nonvanishing off-diagonal $C_{kk'}$ coefficients are smaller than the corresponding C_{kk}^{bulk} expressions by a factor of $2/\pi$. The key effect here is that when the direction of the **k** vector corresponds to standing modes, the $C_{kk'}$ coupling coefficient is nonvanishing only for adjacent standing-mode k values and the value of the coefficient is reduced by a factor of $2/\pi$.

The infinite film theory may be modified to include the lateral film dimensions in a straightforward manner. One simply applies the same $2/\pi$ reduction factor and the same selection rule introduced above to each of the lateral directions. The lateral standing modes have wave-vector y and z components given by $k_y=n_y\pi/L_y$ and $k_z=n_z\pi/L_z$, where n_y and n_z are positive integers and L_y and L_z denote the y and z dimensions of the rectangular sample. Based on the prescription of Refs. 12 and 13, one may immediately write an expression for the lateral coupled mode $C_{kk'}$ coefficients as

$$C_{kk'}=C_{kk}^{\text{bulk}}(2/\pi)^2\left[\frac{1}{n_y-n_y'}\right]\left[\frac{1}{n_z-n_z'}\right]\delta_{n_y-n_y',\text{odd}}\,\delta_{n_z-n_z',\text{odd}}\ . \tag{10}$$

Because there are two lateral mode directions, there are *two* factors of $2/\pi$ and *two* δ functions. While the justification for Eq. (10) given here is heuristic in nature, the same result can be obtained rigorously if one takes the form of the integral of Eq. (26) in Ref. 12, but does lateral direction y and z integrations instead of the perpendicular-to-film direction integration in the paper. As in Ref. 12, one then omits higher-order couplings for mode pairs with $|n_y-n_y'|$ or $|n_z-n_z'|$ greater than 1. This approximation changes the two "odd" arguments of the δ function in Eq. (10) to "±1" arguments. Equation (10) with this modification, along with Eq. (1), constitutes the key working equation for the coupled lateral mode theory.

The coupled mode instability problem defined by Eqs. (1) and (10), along with the other supporting equations in Sec. III A, is not amenable to solution in terms of a simple closed-form threshold equation such as the $h_c^{\text{bulk}}=\eta_k/|C_{kk}^{\text{bulk}}|$ relation obtained in the bulk limit formulation. Rather, it is necessary to consider some specific number of coupled modes close to a specific $(\omega_k=\omega_p/2,k,\theta_k)$ operating point, and determine the microwave field instability threshold amplitude h_c^{film} for that particular operating point numerically. Given this threshold, one would then proceed to obtain $h_{\text{crit}}^{\text{film}}$ as the minimum value of h_c^{film} among all the available $(\omega_k=\omega_p/2,k,\theta_k)$ states for a given value of the field H. This repetitive procedure is tedious at best, and contains little physical insight into the effect of the coupling between the lateral standing-wave modes on the instability processes. As an alternative, a somewhat more insightful solution procedure has been developed. This procedure combines specific aspects of the coupled mode problem with basic properties of the lateral modes to yield a working equation which is similar to the $h_c^{\text{bulk}}=\eta_k/|C_{kk}^{\text{bulk}}|$ bulk limit result. This procedure is described below.

Consider, as a starting point, the explicit lateral standing-mode wave-vector components k_y and k_z for a rectangular sample of side lengths L_y and L_z. These k_y and k_z components will follow the usual behavior for a rectangular box, according to

$$k_y=n_y\pi/L_y \tag{11}$$

and

$$k_z=n_z\pi/L_z\ . \tag{12}$$

As already indicated, the out-of-plane wave-vector component, k_x, is taken to be zero. For a given $N\times N$ cluster of such lateral modes centered at some $(\omega_K=\omega_p/2,K,\theta_K)$ operation point, the modes may be depicted as shown in Fig. 3. The plot shows solid dots in a 6×6 rectangular array on a k_y-k_z reciprocal-lattice plot. The wave number and propagation angle for the spin-wave operating point at the center of the array are now indicated by the parameters K and θ_K, respectively. A capital K and θ_K notation is used here in order to distinguish the k and θ_k operating point parameters from the k and θ_k parameters for the actual standing-wave modes in the array. The objective here is to apply Eq. (1) to such an array of coupled modes, incorporate the $C_{kk'}$ coupling coefficient of Eq. (10) into the problem for a specific static field H, and determine the threshold value of the microwave field amplitude h, taken as h_c^{film}, for the b_k amplitudes to exhibit instability. Of course, one could

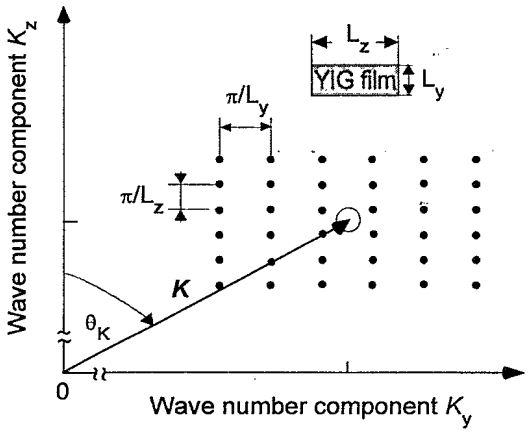

FIG. 3. Schematic reciprocal lattice wave vector diagram showing a 6×6 array of lateral standing-wave modes for a YIG film. The solid dots indicate the discrete standing-wave k_y and k_z wave-number components for the array, centered at a wave number K and polar propagation angle θ_K. The k_y and k_z separations of the mode points are shown as π/L_y and π/L_z, respectively, where L_y and L_z are the y and z dimensions of the rectangular YIG film shown in the inset.

use an array of larger dimension than 6, or use a cluster of different shape. The numerical results obtained below indicate that a 6×6 array is adequate to come within a few percent of the results for an infinite-size cluster of coupled modes.

Once a procedure to obtain h_c^{film} is established, the remaining steps are the same as for previous butterfly-curve evaluations. Recall that h_c^{film} is the instability threshold for the given $(\omega_K=\omega_p/2,K,\theta_K)$ operating point at a specific value of the static field H. One obtains the actual threshold $h_{\text{crit}}^{\text{film}}$ by scanning the available $(\omega_K=\omega_p/2,K,\theta_K)$ states for the given H and finding the minimum h_c value. The range of this scan is determined by the $\omega_K=\omega_p/2$ condition and the dispersion equation of Eq. (7). One then varies the field H and obtains a full butterfly curve. These steps are described in detail in Ref. 9.

Given an $N\times N$ array of coupled modes of the sort shown in Fig. 3 for $N=6$, the next step is to set up the ensemble of coupled equations contained in Eq. (1) for the various b_k and $b_{k'}$ amplitudes included in the array. It will prove notationally convenient to use three integer indices to set up the problem. First, a pair of the I and J indices which both range from 1 to N will be used to scan the locations of the individual modes in the array. There are N^2 such modes. Second, a separate integer index Q will be used to scan the specific (I,J) modes involved in a given ensemble of equations. The number of such modes, denoted as $Q_{\max}$, is not equal to N^2, as one might expect if all of the (I,J) pairs were involved. The selection rules contained in the δ functions of Eq. (10) limit the number of modes which participate in the ensemble of coupled equations contained in Eq. (1). When N is even, Q will range from 1 to $Q_{\max}=N^2/2$. When N is odd, Q will range from 1 to $Q_{\max}=(N^2\pm1)/2$, depending on setup of the coupled equations. These points will be considered shortly.

It is important to note, as well, that the b_k amplitudes are complex. With these amplitudes now specified as b_Q rather than b_k, the complex form of these amplitudes may be expressed according to $b_Q=b_{Qr}+ib_{Qi}$, where the b_{Qr} and b_{Qi} are both real. Insofar as b_{Qr} and b_{Qi} are independent parameters, this means that there will actually be $2Q_{\max}$ equations in $2Q_{\max}$ amplitude parameters. For the 6×6 array in Fig. 3, one has $2Q_{\max}=36$ and 36 coupled equations in 36 unknowns. In order to keep the analytical presentation tractable, some of the basic equations given below will be developed for the simpler 2×2 case. The actual h_c^{film} results in Sec. III C and the butterfly-curve calculations presented in Sec. IV will make use of numerical results obtained for a 6×6 array.

The 6×6 array of modes shown in Fig. 3 is shown in more detail in Fig. 4. Additional scales give the I and J mode indices, ordered in terms of increasing k_y and k_z. The mode points for which the $(I+J)$ sum is odd are shown as solid circles. These "odd sum" mode points are numbered 1–18 and adjacent points are connected by diagonal lines. The mode points for which the $(I+J)$ sum is even are indicated by the × symbols. The distinction between these two types of modes will be made clear shortly. The open diamond at the center of the array designates the nominal $(\omega_K=\omega_p/2,K,\theta_K)$ parametric spin-wave operating point with the frequency at $\omega_K=\omega_p/2$ and the $K-\theta_K$ connection determined from Eq. (7) with k replaced by K. It is assumed that all the modes in the array are close in wave vector and frequency to this operating point. In the context of Eqs. (11) and (12), this means that $n_y\gg I$ and $n_z\gg J$ are satisfied. For

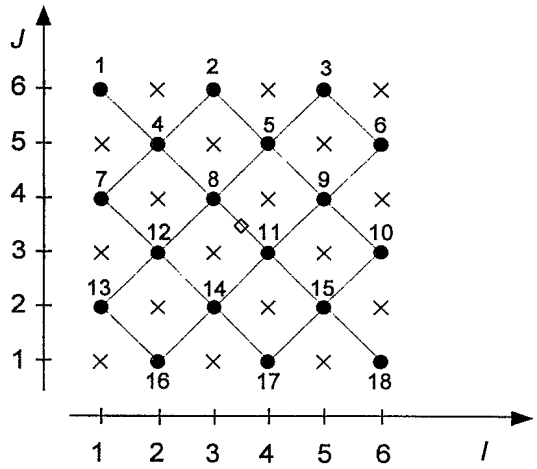

FIG. 4. Schematic wave vector diagram showing the 6×6 array of lateral standing-wave modes centered at a wave number K and polar propagation angle θ_K in a k_y-k_z plot, as in Fig. 3, but in more detail. Additional horizontal and vertical scales show I and J indices for the modes. The solid circles and crosses indicate modes for which the $(I+J)$ index sums are odd and even, respectively. The odd sum modes are also numbered from 1 to 18 and are connected by diagonal lines to indicate the coupling between the connected modes.

sample dimensions of 1–2 mm, this corresponds to wave numbers greater than 100 cm^{-1}. The numerical results to be presented in the next section indicate critical-mode wave numbers of 10^4 cm^{-1} or greater, well beyond this limit on K.

Now consider the application of Eqs. (1) and (10) to the array of modes in Fig. 4. From the δ-function selection rules in Eq. (10), only modes with I indices which differ by 1 and J indices which also differ by 1 will have nonzero $C_{kk'}$ coupling coefficients. This means that only those mode pairs in the array in Fig. 4 which are connected by diagonal lines will be coupled together. This diagonal coupling restriction separates the 36 modes in the 6×6 array into two separate uncoupled subarrays containing 18 modes each. The solid circle points designate one of these subarrays; the × symbols designate the other subarray. Either one of these subarrays may be used to obtain h_c^{film}. As already indicated, $N=6$ is sufficient to achieve threshold field values within a few percent of the large-N limit. For purposes of illustration, the discussion below will focus on the odd sum solid circle mode points in Fig. 4. The numbering of these modes from 1 to 18 indicates the $Q_{\max}=18$ modes which will be involved in the equation set implied from Eq. (1).

Just as Fig. 4 shows the various $\mathbf{k}$ values for the array of coupled lateral modes under consideration here, it is also necessary to know the frequencies for these modes, to be denoted by ω_Q. The ω_Q may be easily expressed in terms of the operating point frequency at the center of the array, $\omega_p/2$, and two additional frequency shift parameters, $\Delta\omega_K$ and Φ_K. These $\Delta\omega_K$ and Φ_K parameters will also play an important role in the final results for the lateral coupled mode thresholds.

Recall, as indicated in Fig. 3, that the change in k_y for a change in the I index of +1 is just $+\pi/L_y$, and similarly, the change in k_z for a change of +1 in the J index is just $+\pi/L_z$. The changes in frequency for a $+\pi/L_y$ change in k_y and a $+\pi/L_z$ change in k_z, for modes close to the $(\omega_K=\omega_p/2,K,\theta_K)$ operating point, are given by

$$\Delta\omega_Y=\left.\frac{\partial\omega_k}{\partial k_y}\right|_{\omega_p/2,K,\theta_K}(\pi/L_y) \tag{13}$$

and

$$\Delta\omega_Z=\left.\frac{\partial\omega_k}{\partial k_z}\right|_{\omega_p/2,K,\theta_K}(\pi/L_z)\,, \tag{14}$$

respectively. If both indices change by +1 at the same time, the net change in frequency would be given by $\delta\omega_k=\Delta\omega_Y+\Delta\omega_Z$. Such a change could correspond, for example, to an outward move from one solid circle mode point in Fig. 4 to another. It is important to note that $\Delta\omega_Y$ scales with π/L_y and $\Delta\omega_Z$ scales with π/L_z. The $\Delta\omega_K$ and Φ_K parameters are introduced to express this frequency shift in polar form, by writing $\Delta\omega_Y=\Delta\omega_K\sin\Phi_K$ and $\Delta\omega_Z=\Delta\omega_K\cos\Phi_K$. One obtains

$$\Delta\omega_K=+\sqrt{(\Delta\omega_Y)^2+(\Delta\omega_Z)^2} \tag{15}$$

and

$$\Phi_K=\tan^{-1}\left[\frac{\Delta\omega_Y}{\Delta\omega_Z}\right]. \tag{16}$$

Note that $\Delta\omega_K$ is defined as positive. These parameters are discussed in detail in the Appendix.

The $(\omega_Q-\omega_p/2)$ frequency shift term for a given Q mode, which corresponds to the $(\omega_k-\omega_p/2)$ term in Eq. (1), may be expressed quite simply in terms of the above parameters. For the $Q=8$ mode in Fig. 4, for example, which is located close to the $\omega_p/2$ operating point at the array center, $(\omega_Q-\omega_p/2)$ is simply equal to $(\Delta\omega_Y-\Delta\omega_Z)/2$ or $\Delta\omega_K(\cos\Phi_K-\sin\Phi_K)/2$. For a general (I,J) point in Fig. 3, $(\omega_Q-\omega_p/2)$ is given by $\Delta\omega_K[(I-3\frac{1}{2})\sin\Phi_K+(J-3\frac{1}{2})\cos\Phi_K]$. The $\Delta\omega_K$ and Φ_K parameters, however, are more than just a convenient way to express mode frequency shifts. These parameters, and $\Delta\omega_K$ in particular, will be central parameters in the solutions to coupled lateral mode problem. Both of these parameters are well-defined functions of ω_p, K, and θ_K, based on the condition $\omega_K=\omega_p/2$ and the dispersion condition of Eq. (7) with k replaced by K. Expressions for $\Delta\omega_K$ and Φ_K are obtained in the Appendix. The $\Delta\omega_K$ expression, given through Eqs. (A7)–(A9) and (A13) will be needed for the numerical evaluations of Sec. IV.

It is useful at this point to consider the functional form of $\Delta\omega_K$ in the limit for which the K dependence of ω_K can be neglected. As also discussed in the Appendix, this is the applicable limit over most of the range of K states considered here. In this limit, one obtains an expression for $\Delta\omega_K$ of the form

$$\Delta\omega_K=\frac{\gamma\omega_m(H+DK^2)}{\omega_p}\frac{\sin(2\theta_K)}{K}\times\sqrt{\sin^2\theta_K(\pi/L_z)^2+\cos^2\theta_K(\pi/L_y)^2}\,. \tag{17}$$

The functional dependences shown in Eq. (17) are of key importance in the coupled mode theory. As will be shown below, the thin-film threshold field h_c^{film} is an increasing function of $\Delta\omega_K/\eta_k$. This means that apart from other $\mathbf{K}$ dependences for the spin-wave linewidth, the various coupling coefficients, etc., the K and θ_k dependences of $\Delta\omega_K$ will also affect the properties of the critical mode with the minimum h_c^{film} at a given field H. Of particular note in this context are the $\sin(2\theta_K)$ and the $1/K$ terms in Eq. (17). As the results of Sec. IV will show, the $\sin(2\theta_K)$ term in $\Delta\omega_K$ has the same general effect on the final critical mode that the *ad hoc* $\sin^2(2\theta_K)$ term in the spin-wave linewidth $\Delta H_k(\mathbf{k})$ function of Eq. (8) had in the bulk theory. This means that one can obtain good theoretical fits to experimental data *without* this *ad hoc* term in $\Delta H_k(\mathbf{k})$. The $1/K$ term in Eq. (17), moreover, adds a coupling preference for high K modes. It is this effect that leads to the critical-mode K values in the 10^4–10^5 cm^{-1} range. These effects will be considered in detail in Sec. IV.

Return to the odd sum mode point subarray in Fig. 4. In order to begin the construction process for the 36 simultaneous equations implicit in this subarray, consider Eq. (1) with the k and k' subscripts replaced by Q and Q'.

The starting point is the same as in the bulk limit case. One assumes some solution for the complex $b_Q(t)$ amplitudes of the form

$$\begin{bmatrix} b_{1r}(t) \\ b_{1i}(t) \\ \cdot \\ \cdot \\ b_{Q_{\max}r}(t) \\ b_{Q_{\max}i}(t) \end{bmatrix} = \begin{bmatrix} b_{1r} \\ b_{1i} \\ \cdot \\ \cdot \\ b_{Q_{\max}r} \\ b_{Q_{\max}i} \end{bmatrix} e^{\beta t} = \mathbf{b}_K e^{\beta t} . \quad (18)$$

The β parameter in Eq. (18) is the same as in Sec. III A. At threshold, with $h = h_c^{\text{film}}$, β will be zero. The procedure for the determination of this condition will be made clear shortly. Recall also that b_Q are complex, according to $b_Q = b_{Qr} + ib_{Qi}$. There are, in general, $2Q_{\max}$ amplitude parameters in the column vector $\mathbf{b}_K$.

Substitution of Eq. (18) into Eq. (1), for all of the odd sum mode points in the array of Fig. 4, leads to an eigenvalue equation of the form $\mathbf{M}_K \cdot \mathbf{b}_K = \beta \mathbf{b}_K$, where $\mathbf{M}_K$ is a 36×36 matrix of real terms and $\mathbf{b}_K$ is a column vector with 36 real amplitude parameters, $b_{1r}, b_{1i}, \ldots, b_{18r}, b_{18i}$. The terms in $\mathbf{M}_K$ involve the various ω_Q mode frequencies, the relaxation rate η_K, the $C_{QQ'}$ coupling coefficients from Eq. (10) for the modes connected by the diagonal lines in Fig. 4, and the microwave field amplitude h. It is clear that even for this modest 6×6 array, the subarray eigenvalue problem is formidable.

In spite of the large dimensionality, however, the solution of this eigenvalue equation for the threshold value of h, h_c^{film}, for the specified $(\omega_K = \omega_p/2, K, \theta_K)$ operating point is, in principle, straightforward. One simply varies h, starting from some low value, solves $\mathbf{M}_K \cdot \mathbf{b}_K = \beta \mathbf{b}_K$ for the $2Q_{\max}$ complex eigenvalues for β, denoted as $\beta_l = \beta_l' + i\beta_l''$, as a function of h. The threshold h_c^{film} is that value of h for which the maximum β_l' value changes from negative to positive. This h_c^{film} threshold amplitude then represents, for the coupled lateral mode problem, the instability point which corresponds to the $\beta = -\eta_k + |C_{kk}^{\text{bulk}}||h| = 0$ condition and $h_c^{\text{bulk}} = \eta_k / |C_{kk}^{\text{bulk}}|$ in the bulk limit.

It has been found, however, that the effect of the lateral mode coupling on the instability threshold can be obtained from the $\mathbf{M}_K$ eigenvalue problem in a much simpler, more useful, and more insightful form than obtained from the above procedure. Specifically, one can obtain numerical solutions for the $h_c^{\text{film}}/h_c^{\text{bulk}}$ ratio as a relatively simple function of the $\Delta\omega_K/\eta_k$ ratio introduced above. This means that the thin-film threshold h_c^{film} as a function of θ_K for fixed H can be written as

$$h_c^{\text{film}} = \frac{\eta_K}{|C_{KK}^{\text{bulk}}|} F(\Delta\omega_K/\eta_K, \Phi_K) , \quad (19)$$

where $F(\Delta\omega_K/\eta_K, \Phi_K)$ represents the functional dependence of $h_c^{\text{film}}/h_c^{\text{bulk}}$ on $\Delta\omega_K/\eta_k$. Recall that for $\omega_K = \omega_p/2$ and H fixed, the dispersion equation of Eq. (7) with k replaced by K leads to a well-defined range for the available θ_K and $K(\theta_K)$ values. This means that all terms on the right-hand side of Eq. (19) can be reduced to relatively simple functions of θ_K only. The $K(\theta_K)$ dependence of η_k comes from the $\Delta H_k(\mathbf{k})$ function in Eq. (7) but without, as already discussed, the *ad hoc* $\sin^2(2\theta_K)$ term. The θ_K dependence of C_{KK}^{bulk} is given through Eq. (2) with θ_k replaced by θ_K. The $K(\theta_K) - \theta_K$ dependence of $\Delta\omega_K$ comes from the full $\Delta\omega_K(K, \theta_K)$ result in the Appendix or the approximate result in Eq. (17).

C. The coupled lateral mode eigenvalue problem simplified

In order to establish the result briefly described above, it is necessary to consider the specific form of the $\mathbf{M}_K \cdot \mathbf{b}_K = \beta \mathbf{b}_K$ eigenvalue problem in detail. Explicit considerations for the full 36×36 matrix problem based on the $N = 6$ odd sum subarray in Fig. 4 would be intractable. For purposes of discussion, the 4×4 matrix problem based on the $N = 2$ case will be used. Consider, therefore, the $Q = 8$ and 11 mode points in Fig. 4 only, along with the diagonal line connecting these two points, and ignore the remainder of the array. For convenience, these $Q = 8$ and 11 mode points will be renumbered as 1 and 2, respectively. Note that the $(\omega_1 - \omega_p/2)$ frequency shift term for this new mode 1 is just $\frac{1}{2}\Delta\omega_K(\cos\Phi_K - \sin\Phi_K)$, the same as in the example given earlier. This frequency shift will be denoted as $\Delta\omega_A$. The $(\omega_2 - \omega_p/2)$ frequency shift term for new mode 2 is $-\Delta\omega_A$. Application of Eq. (1) to these two coupled modes only yields two coupled complex equations given by

$$\dot{b}_1(t) = -(\eta_k + i\Delta\omega_A) b_1(t) - h(2/\pi)^2 C_{KK}^{\text{bulk}} b_2^*(t) \quad (20)$$

and

$$\dot{b}_2(t) = -(\eta_k + i\Delta\omega_A) b_2(t) - h(2/\pi)^2 C_{KK}^{\text{bulk}} b_1^*(t) . \quad (21)$$

One then invokes the explicit complex form for the b_1 and b_2 already specified, assumes a time dependence as in Eq. (18), and then constructs an eigenvalue problem in the form $\mathbf{M}_k \cdot \mathbf{b}_K = \beta \mathbf{b}_K$. The $\mathbf{M}_K$ matrix for the 4×4 problem is given by

$$\mathbf{M}_K = \begin{bmatrix} -\eta_K & +\Delta\omega_A & -hC_{KK}^{\text{bulk}}(2/\pi)^2 & 0 \\ -\Delta\omega_A & -\eta_K & 0 & +hC_{KK}^{\text{bulk}}(2/\pi)^2 \\ -hC_{KK}^{\text{bulk}}(2/\pi)^2 & 0 & -\eta_K & -\Delta\omega_A \\ 0 & +hC_{KK}^{\text{bulk}}(2/\pi)^2 & +\Delta\omega_A & -\eta_K \end{bmatrix} . \quad (22)$$

The $\mathbf{b}_K$ vector is now a four-component eigenvector. The $\mathbf{M}_K \cdot \mathbf{b}_K = \beta \mathbf{b}_K$ condition amounts to a homogeneous set of four equations in four unknowns, in the form $(\mathbf{M}_K - \beta \mathbf{N}) \cdot \mathbf{b}_K = 0$, where $\mathbf{N}$ is a diagonal 4×4 unit matrix. The requirement for nontrivial solutions for $\mathbf{b}_K$ is $|\mathbf{M}_K - \beta \mathbf{N}| = 0$. From the form of Eq. (22), this $|\mathbf{M}_K - \beta \mathbf{N}| = 0$ condition constitutes a quartic equation in β with four roots, β_1, β_2, β_3, and β_4. These roots are the four eigenvalues of the problem. As already discussed, the general procedure would be (1) to select some particular field H and specific $(\omega_K = \omega_p/2, K, \theta_K)$ operating point, (2) obtain numerical values for $\Delta\omega_A$ and C_{KK}^{bulk}, (3) include suitable numerical parameters in the spin-wave linewidth equation and determine η_K, (4) evaluate the four complex β values as a function of increasing h, and (5) obtain h_c^{film} as that value of h for which the maximum value among $\text{Re}\beta_1$, $\text{Re}\beta_2$, $\text{Re}\beta_3$, and $\text{Re}\beta_4$, changes from negative to positive. Even for this 4×4 system, such a procedure is tedious and complicated.

There is a much simpler procedure to obtain threshold fields from Eq. (22). This procedure is based on two realizations about the solutions to the above eigenvalue problem. The first of these concerns the general form of the h_c^{film} solution. Consider the effect of dividing both sides of the $\mathbf{M}_K \cdot \mathbf{b}_K = \beta \mathbf{b}_K$ equation by η_K to obtain $(\mathbf{M}_K/\eta_K) \cdot \mathbf{b}_K = (\beta/\eta_K)\mathbf{b}_K$. This simple change has important consequences. The elements in the $\mathbf{M}_K/\eta_K$ matrix involve only two types of terms, one term of the form $(\Delta\omega_A/\eta_K)$ and the other of the form $(hC_{KK}^{\text{bulk}}/\eta_K)$. The value of h at which the zero crossing for the maximum value among of $\text{Re}(\beta_1/\eta_K)$, $\text{Re}(\beta_2/\eta_K)$, $\text{Re}(\beta_3/\eta_K)$, and $\text{Re}(\beta_4/\eta_K)$ occurs will be the same as before, since the zero crossing is unaffected by a division by η_K. This means that when the zero crossing is determined, one will have determined $(h_c^{\text{film}} C_{KK}^{\text{bulk}}/\eta_K)$ for the corresponding value of $(\Delta\omega_A/\eta_K)$ which was used in the matrix $\mathbf{M}_K/\eta_K$. Recall, however, that the corresponding threshold in the bulk limit, h_c^{bulk}, is just $\eta_K/|C_{KK}^{\text{bulk}}|$. Since the frequency shift parameter $\Delta\omega_A$ is equal to $\frac{1}{2}\Delta\omega_K(\cos\Phi_K - \sin\Phi_K)$, one has the rather powerful result that the ratio of the thin-film threshold which takes the coupled lateral modes into account to the same threshold in the bulk limit, $h_c^{\text{film}}/h_c^{\text{bulk}}$, is simply a function of the $\Delta\omega_K/\eta_K$ ratio with Φ_K as a parameter. The $F(\Delta\omega_K/\eta_k, \Phi_K)$ function introduced in Eq. (19) denotes this functional dependence. This is a general result for any size array. In the limit of large N, the corresponding $F(\Delta\omega_K/\eta_k, \Phi_K)$ represents the effect of the lateral mode coupling on the threshold.

The second realization concerns a much less tedious procedure to determine $h_c^{\text{film}}/h_c^{\text{bulk}}$ as a function of the $\Delta\omega_K/\eta_K$ ratio, compared to the iterative, zero-crossing method described above. It is actually necessary to consider only *one* set of eigenvalues for *one* somewhat arbitrary choice of numerical values for the $\Delta\omega_K$ and $[hC_{KK}^{\text{bulk}}(2/\pi)^2]$ elements in $\mathbf{M}_K$ in order to determine one pair of values for $h_c^{\text{film}}/h_c^{\text{bulk}}$ and $\Delta\omega_K/\eta_K$ at a given value of Φ_K. This greatly simplifies the threshold determination problem. Then, by varying the numerical values for $\Delta\omega_K$ and $hC_{KK}^{\text{bulk}}(2/\pi)^2$ over some range, one can construct a more-or-less general curve of $h_c^{\text{film}}/h_c^{\text{bulk}}$ as a function of $\Delta\omega_K/\eta_K$. The $F(\Delta\omega_K/\eta_k, \Phi_K)$ introduced in Eq. (19) corresponds to this general curve. The details of the procedure and specific $F(\Delta\omega_K/\eta_k)$ functions are discussed below.

Just as the result on functional dependences came from dividing $\mathbf{M}_K$ by η_K, the above result on single eigenvalue solutions for $h_c^{\text{film}}/h_c^{\text{bulk}}$ as a function of $\Delta\omega_K/\eta_K$ derives from adding a term $\eta_K \mathbf{I}$ to $\mathbf{M}_K$. Note that the $\mathbf{M}_K$ matrix in Eq. (22) contains diagonal terms which are all the same and equal to $-\eta_K$. If one adds a diagonal matrix $\eta_K \mathbf{I}$ to $\mathbf{M}_K$ and replaces β by $(\beta + \eta_K)$, the $\mathbf{M}_K \cdot \mathbf{b}_K = \beta \mathbf{b}_K$ eigenvalue equation may be rewritten in the form

$$(\mathbf{M}_K + \eta_K \mathbf{I}) \cdot \mathbf{b}_K = \mathbf{R}_K \cdot \mathbf{b}_K = (\beta + \eta_K)\mathbf{b}_K = \rho \mathbf{b}_K \,. \quad (23)$$

The matrix $\mathbf{R}_K$ is the same as $\mathbf{M}_K$ but with only zeros along the diagonal. The η_K parameter is no longer contained in the matrix. Further note that when, in the zero-crossing solution process described above, the maximum value among $\text{Re}\beta_1$, $\text{Re}\beta_2$, $\text{Re}\beta_3$, and $\text{Re}\beta_4$ changes from negative to positive, the maximum value among $\text{Re}\rho_1$, $\text{Re}\rho_2$, $\text{Re}\rho_3$, and $\text{Re}\rho_4$ will be equal to η_K.

Based on Eqs. (22) and (23), one may determine $h_c^{\text{film}}/h_c^{\text{bulk}}$ as a function of $\Delta\omega_K/\eta_k$, with Φ_K as a parameter, in a very simple manner. The procedure is as follows: (1) Choose some value for Φ_K for the overall curve. (2) Pick some reasonable numerical value W to serve as an operational value for $\Delta\omega_K$ and evaluate the corresponding value for

$$\Delta\omega_A = \tfrac{1}{2}\Delta\omega_K(\cos\Phi_K - \sin\Phi_K) = A(W, \Phi_K) \,.$$

(3) Pick some reasonable numerical value V to serve as an operational value for the combination of parameters $[hC_{KK}^{\text{bulk}}(2/\pi)^2]$. (4) Solve the eigenvalue problem of Eq. (23) for four eigenvalues of ρ, and then select the maximum value among $\text{Re}\rho_1$, $\text{Re}\rho_2$, $\text{Re}\rho_3$, and $\text{Re}\rho_4$. Let this value be denoted as R. The key connection, once these calculations have been done, is to realize that R is related to η_K. This R value represents the value of η_K for which the maximum value among $\text{Re}\beta_1$, $\text{Re}\beta_2$, $\text{Re}\beta_3$, and $\text{Re}\beta_4$ would cross zero for the combination of parameters imbedded in W and V. One can write, therefore, $h_c^{\text{film}}/h_c^{\text{bulk}} = (\pi/2)^2 V$ and $\Delta\omega_K/\eta_k = W/R$. In order to generate the $F(\Delta\omega_K/\eta_k, \Phi_K)$ function for the chosen Φ_K value, one simply scans over some suitable range of numerical values for W and V, follows the procedure described above, and obtains $h_c^{\text{film}}/h_c^{\text{bulk}}$ as a function of $\Delta\omega_K/\eta_k$. By repeating the entire procedure for different values of Φ_K, one generates operational curves for the function $F(\Delta\omega_K/\eta_k, \Phi_K)$.

It is important to emphasize the simplicity of the above procedure. First, one may note that it is not necessary to select any particular $(\omega_K = \omega_p/2, K, \theta_K)$ operating point to determine the functional dependences for $F(\Delta\omega_K/\eta_k, \Phi_K)$. Once these functional dependences have been obtained, however, one may return to the operating point perspective to determine h_c^{film} according to Eq. (19). Of particular note is the extremely simple form of the operational eigenvalue problem. In terms of

the above parameters, the eigenvalue problem is expressed simply as

$$\begin{vmatrix} -\rho & +\Omega & -V & 0 \\ -\Omega & -\rho & 0 & +V \\ -V & 0 & -\rho & -\Omega \\ 0 & +V & +\Omega & -\rho \end{vmatrix} = 0 , \tag{24}$$

where $\Omega = \frac{1}{2}W(\cos\Phi_K - \sin\Phi_K)$, W and V are just scanned numbers and ρ represents the four roots of the quartic equation implicit in the 4×4 determinant. As such, the approach is readily extended to larger subarrays. For larger arrays, such as the $N=6$ array in Figs. 3 and 4, there will be two different Ω functions rather than one, since there will be coupled modes for the two different diagonal directions rather than the one 8–11 connection used in Fig. 4 for the two-mode case. Other than this difference, along with the higher dimensionality of the determinant, the problem for larger arrays is the same as for the two-mode case.

Based on the above procedure, numerical point-by-point constructions for $F(\Delta\omega_K/\eta_k, \Phi_K)$ as a function of $\Delta\omega_K/\eta_k$ with Φ_K as a parameter have been done for cases up to $N=6$. For the purposes of these calculations, the V parameter in Eq. (24) was set equal to 1. The scanning was accomplished by fixing Φ_K and changing W to vary Ω. Typical values for W ranged from 0 to 100 MHz. Results for the $N=6$ case are shown in Fig. 5. The various solid curves show values of $F(\Delta\omega_K/\eta_k, \Phi_K)$ as a function of $\Delta\omega_K/\eta_k$ for different choices of Φ_K. The dashed curve labeled G represents a fitted function to be discussed shortly. The inset diagram shows limiting F values for in the limit of large $\Delta\omega_K/\eta_k$ as a function of Φ_K. The notches shown in the inset have special significance, to be discussed shortly.

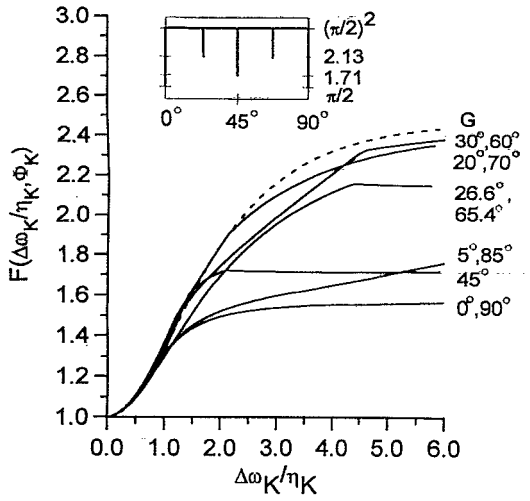

FIG. 5. Curves of the $h_c^{\text{film}}/h_c^{\text{bulk}}$ functions $F(\Delta\omega_K/\eta_k, \Phi_K)$ and $G(\Delta\omega_K/\eta_k)$ as a function of $\Delta\omega_K/\eta_k$. The solid lines show F curves for various values of Φ_K as indicated. The dashed line shows the G curve. The inset shows, in schematic form, the limiting values of F obtained for large values of $\Delta\omega_K/\eta_k$ on the order of 100, as a function of Φ_K. The notches for Φ_K equal to the special angles of 0°, 26.6°, 45°, 65.4°, and 90° indicate special limits as shown.

One result evident from Fig. 5 is the common functional dependence on $\Delta\omega_K/\eta_k$ for all the F curves, regardless of Φ_K, for values of $\Delta\omega_K/\eta_k$, below 1 or so. In this low $\Delta\omega_K/\eta_k$ range, the solid F curves all lie more-or-less together and show very little dependence on Φ_K. This commonality will be important for butterfly-curve calculations. In the limit $\Delta\omega_K/\eta_k \to 0$, all the F curves go to 1. This corresponds, of course, to thin-film thresholds going over to the bulk limit. This result is physically reasonable and provides one check on the calculation. In the $\Delta\omega_K/\eta_k \to 0$ limit, all the coupled modes are very close together and correspond, more-or-less, to a single bulk mode at $(\omega_K = \omega_p/2, K, \theta_K)$.

For values of $\Delta\omega_K/\eta_k$ greater than 1, the various F curves show significantly different behaviors. The curves show a Φ_K symmetry about 45°, that is, curves for 0° and 90°, 20° and 70°, 26.6° and 65.4°, etc., are identical. The curves for the special Φ_K values of 26.6°, 30°, 45°, etc., show kinks. The curves for the other angles shown show relatively smooth increases in F with $\Delta\omega_K/\eta_k$. All curves, with the possible exception of the 5° and 85° curves, show evidence of leveling off at high $\Delta\omega_K/\eta_k$.

All curves do, in fact, level off for $\Delta\omega_K/\eta_k$ above 10–100 or so, depending on Φ_K. The inset in Fig. 5 shows these F limits. This inset diagram shows that the limiting value of F for a general value of Φ_K, with the exception of five special angles, is 2.47. The special limits for $\Phi_K = 0°$, 24.6°, 45°, and the compliments of these angles are indicated by the notches in the inset diagram. At 0° and 90°, the F limit is 1.57. At 24.6° and 65.4°, the F limit is about 2.13. At 45°, the limit is about 1.71. These limiting values provide important checks on the theory, to be considered shortly.

The results in Fig. 5 reveal both the simple and the complex aspects of the lateral coupled mode problem. The simple aspect of the problem is in the single functional dependence of F on $\Delta\omega_K/\eta_k$ which is more or less independent of Φ_K when $\Delta\omega_K/\eta_k$ is less than 1 or so. This result makes intuitive sense. Recall that the relaxation rate η_k represents, in essence, the frequency broadening for any given mode. When $\Delta\omega_K/\eta_k < 1$ is satisfied, such broadening dominates over any directional dependent reciprocal-lattice effects for the severely overlapping modes.

In the opposite limit of large $\Delta\omega_K/\eta_k$, on the other hand, the results in Fig. 5 show that the variation in F with $\Delta\omega_K/\eta_k$ changes significantly for different values of Φ_K. From the curves in Fig. 5, it would appear that different Φ_K values not only yield different limiting values for F at very high $\Delta\omega_K/\eta_k$, but also result in very different functional dependences as well. Closer inspection of the various curves, however, reveals several patterns which relate to the fundamental considerations presented above. First, note that the F values in the limit of large $\Delta\omega_K/\eta_k$, except for the special angles, are all close to $(\pi/2)^2$. Values of F at $\Delta\omega_K/\eta_k \approx 100$, for example, for values of Φ_K away from the special angles already indicated, were all within 0.3% of $(\pi/2)^2 \approx 2.4674$. Re-

call that $1/(\pi/2)^2$ is the numerical factor involved in the $C_{kk'}$ coupling coefficients in the lateral mode problem. In the limit of large $\Delta\omega_K/\eta_k$, the threshold is increased by a factor of $(\pi/2)^2$.

The limits for the special angles already noted are also of interest. At $\Phi_K=0°$ or 90°, for example, the corresponding curves in Fig. 5 level off at a much lower value of F on the order of 1.6. The numerical evaluations yielded $F=1.5691$ for $\Delta\omega_K/\eta_k\approx 10$. This is within about 0.1% of $\pi/2$. These Φ_K values of 0° or 90°, however, correspond to a *single* lateral standing-mode direction along y or z only. This is due to the fact that for $\Phi_K=0°$, $\Delta\omega_Y$ is zero, and for $\Phi_K=90°$, $\Delta\omega_Z$ is zero. For a single standing-mode direction, one has the same situation as for single standing modes across the film cross section and considered in Ref. 13. In this case, the coupling factor is reduced by one power of $(2/\pi)$ only and the threshold should be increased accordingly. The fact that the numerical evaluations for the $N=6$ array yield F limits at large $\Delta\omega_K/\eta_k$ which agree with the basic starting points for the theory, both for the general angle case cited above and for the special 0° and 90° cases just discussed, provides a good test of the entire procedure. This also shows that the coupled modes are fairly localized around the $(\omega_K=\omega_p/2,K,\theta_K)$ operating point.

There are other special angles as well. At $\Phi_K=45°$, the mode pairs for which the J index decreases and the I index increases by one unit are all at the same frequency. At this special angle, the calculated F value for $\Delta\omega_K/\eta_k=10$ was 1.715. After considering various trial functions involving $\pi/2$, one finds that this value is fairly close to

$$\tfrac{1}{2}\sqrt{[(\pi/2)^2]^2+[(\pi/2)^2]^2}=\frac{1}{\sqrt{2}}(\pi/2)^2\approx 1.75 \ .$$

This limit may correspond to some sort of averaged geometric mean coupling factor. For $\Phi_K\approx 26.6°$, which corresponds to $\tan\Phi_K=\frac{1}{2}$, the calculated F value at $\Delta\omega_K/\eta_k=85$ is close to 2. These special limits are most likely related to special coupling considerations. The physical significance of these limits has not been studied in detail.

As the results in the next section on threshold fields will show, the critical modes with the lowest threshold generally fall in the range where $\Delta\omega_K/\eta_k$ is less than unity, and not in the range of large $\Delta\omega_K/\eta_k$ where the dependences of F on Φ_K become critical. This means that the choice of Φ_K should not be critical to the butterfly-curve calculations of interest. On the basis of the low $\Delta\omega_K/\eta_k$ portion of the curves shown in Fig. 5 and the general angle limiting F value of $(\pi/2)^2$ for large $\Delta\omega_K/\eta_k$, an operational Φ_K-independent G curve has been adopted in place of the Φ_K-dependent F curves in Fig. 5 for the purposes of butterfly-curve evaluations. This G curve was constructed in terms of a $G(\Delta\omega_K/\eta_k)$ function given by

$$G(\Delta\omega_K/\eta_K)=(\pi/2)^2-\frac{(\pi/2)^2-1}{\cosh(\frac{3}{4}\Delta\omega_K/\eta_K)} \ . \qquad (25)$$

The two $(\pi/2)^2$ terms in Eq. (25), in combination with the cosh function, force the function to approach the appropriate limits $G=1$ for $\Delta\omega_K/\eta_k\to 0$ and $G=(\pi/2)^2$ for $\Delta\omega_K/\eta_k\gg 1$. The $\frac{3}{4}$ multiplier inside the cosh function gives a good overall fit to the F curves at $\Delta\omega_K/\eta_k=1$. The dashed curve labeled G in Fig. 5 indicates the functional dependence of Eq. (25).

The above results provide the framework for thin-film butterfly-curve calculations which take coupled lateral modes into account. Based on the G function defined above, it is now a straightforward matter to evaluate the film spin-wave-instability threshold microwave field amplitude for a given field H and $(\omega_K=\omega_p/2,K,\theta_K)$ operating point. This threshold now can be written in simple form, according to

$$h_c^{\text{film}}=\frac{\eta_K}{|C_{KK}^{\text{bulk}}|}G(\Delta\omega_K/\eta_K) \ . \qquad (26)$$

The minimum threshold $h_{\text{crit}}^{\text{film}}$ is then obtained by scanning K and θ_K over their allowed ranges of values, based on the dispersion constraint of Eq. (7) with k replaced by K and ω_K set to $\omega_p/2$, and evaluating

$$h_{\text{crit}}^{\text{film}}=\min(h_c^{\text{film}}|_{\omega_K=\omega_p/2}) \ . \qquad (27)$$

The "min" function in Eq. (27) denotes taking the smallest value of h_c^{film} obtained through Eq. (26), subject to the constraint on the available $(\omega_K=\omega_p/2,K,\theta_K)$ modes. This minimum threshold should then correspond to the measured threshold h_{crit} for the given H. Theoretical butterfly curves may then be obtained by varying H over the experimental range and evaluating $h_{\text{crit}}^{\text{film}}$ as a function of field.

The butterfly-curve calculation procedure just described follows the approach used by Patton and Jantz and earlier workers. The new result is contained in the G-function multiplier in Eq. (26) which models the effect of the lateral standing-mode couplings on the thin-film threshold. The $\Delta\omega_K$ parameter which drives this G function has functional dependences on K and θ_K shown in Eq. (17). Both the inverse K dependence and the $\sin(2\theta_K)$ dependence in Eq. (17) will prove critical to the computed butterfly curves and critical-mode results to be presented shortly. The remaining $\eta_K/|C_{KK}^{\text{bulk}}|$ term on the right-hand side of Eq. (26) represents the bulk limit result. The C_{KK}^{bulk} coefficient is given in Eq. (2). The relaxation rate η_K, as already indicated, may be expressed in terms of a $\mathbf{K}$-dependent spin-wave linewidth according to $\Delta H_K=2\eta_K/\gamma$. Now, however, ΔH_K may be taken to have a strict three-magnon form according to

$$\Delta H_k(\mathbf{k})=A_0+B_1L(k/k_c) \ . \qquad (28)$$

Because of the $\sin(2\theta_K)$ factor already contained in $\Delta\omega_K$, it is no longer necessary to include an *ad hoc* $\sin^2(2\theta_K)$ term in ΔH_K as contained in Eq. (8). As the results of the next section will show, the above operational formulas allow one to (a) model the orientation effect on the butterfly curves which is found experimentally and shown in Fig. 1 and (b) obtain critical modes which show the kink effect and have wave numbers for H values above the kink

point which are in the 10^4-10^5 cm^{-1} range found experimentally by Brillouin light scattering.

IV. BUTTERFLY-CURVE COMPUTATIONS

The butterfly-curve data presented in Sec. II and as shown in Fig. 1 have been used as a basis for theoretical fits, following the development summarized in Sec. III. The calculated butterfly curves were obtained from Eq. (27), with other parameters and expressions as defined and discussed above. Apart from the materials and experimental parameters already assigned numerical values, the only remaining parameters are the spin-wave parameters A_0, B_1, and k_c. These three parameters were treated as adjustable parameters and used to obtain calculated butterfly curves which best matched the data. Representative results are shown in Figs. 6 and 7. Figure 6 shows calculated butterfly curves for the long and short configurations used for the measurements presented in Sec. II. Figure 7 shows the calculated butterfly curve for the long configuration, along with the data from Fig. 1, and companion graphs on the critical mode K and θ_K values vs field which correspond to these thresholds. The values of A_0, B_1, and k_c for the calculated curves in Figs. 6 and 7 were 0.35 Oe, 0.58 Oe, and 8.5×10^5 cm^{-1}, respectively. These A_0 and B_1 values are in the same range as the A_0 and B_1 values in Refs. 6 and 13. The actual values are different because the fits here were based on a ΔH_K function of the form specified in Eq. (28) and the thin-film theory. The fits in Refs. 6 and 13 were based on a ΔH_K function of the form given in Eq. (8) and the bulk theory. The selected value of k_c is the same as the Spark's theoretical value cited in Ref. 6.

The results shown in Fig. 6 constitute the main evidence for the applicability of the coupled lateral mode model to the thin-film data in Fig. 1. The calculated butterfly curves for the long and the short configurations

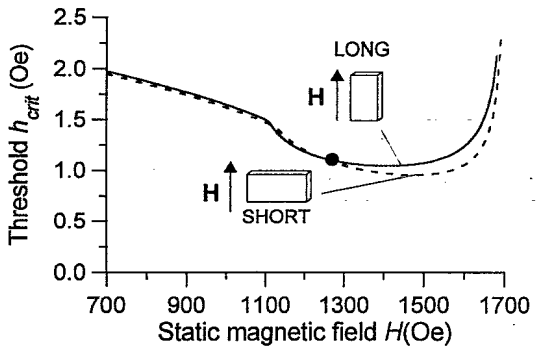

FIG. 6. Calculated subsidiary absorption butterfly curves of the spin-wave-instability threshold h_{crit} as a function of the static external field H for the case of in-plane and mutually perpendicular static and microwave fields, a 1.1 by 2.0 mm yttrium iron garnet thin film, and a pump frequency of 9.4 GHz. The solid curve corresponds to the long configuration, with H parallel to the long edge of the rectangular film. The dashed curve corresponds to the short configuration, with H parallel to the short edge of the film. The solid dot marks the crossover point between the two curves at $H\approx1250$ Oe.

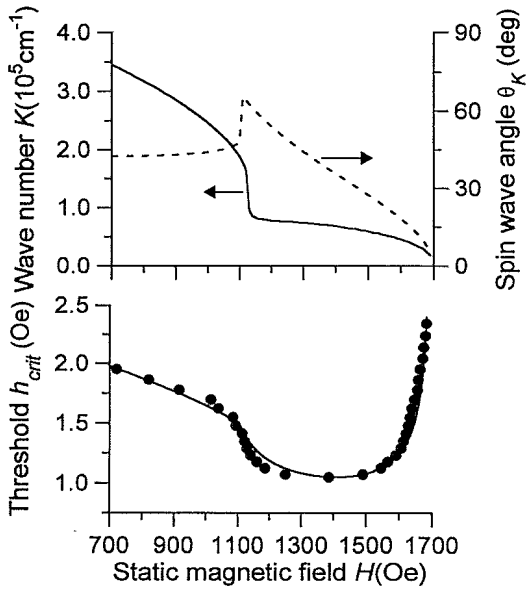

FIG. 7. Experimental data on the spin-wave-instability threshold h_{crit} as a function of the static external field H from Fig. 1 for the long configuration and the theoretical fit to those data from Fig. 6, with companion plots of the corresponding theoretical critical mode spin wave number K and polar angle θ_K parameters versus static external field H.

are shown by the solid and dashed line curves, respectively. The crossover point between the two curves is indicated by a solid dot at $H=1250$ Oe. These curves reproduce the same basic differences evident from the data. The kink for the short configuration occurs at a slightly higher static field, just as in the experiment. At higher fields, the h_{crit} values for the short configuration also fall below those for the long configuration, the same effect evident from the data. These differences are attributed, therefore, to the differences in the lateral standing modes for the two configurations. A key quantitative connection with the data comes from the crossover point. From the theory, this crossover corresponds to a critical model at $\theta_K\approx45°$. From Eq. (17), 45° is the critical mode angle for which L_y and L_z may be interchanged without affecting $\Delta\omega_K$. Recall that the crossover in the data also indicated a critical mode angle close to 45°.

Turn now to the results in Fig. 7. The lower portion of the figure shows the data points and calculated butterfly curve for the long configuration. The upper portion of the figure shows companion plots of the corresponding theoretical critical-mode spin-wave wave vector K and spin-wave angle θ_K values vs H. The good match between the fitted butterfly curve and the data in the lower part of the figure is clear. The fit is somewhat better than that obtained in Ref. 13. This better fit, moreover, is obtained with the ΔH_K function of Eq. (28), without recourse to the additional *ad hoc* $\sin^2(2\theta_K)$ used in Refs. 6 and 13. Such a term is no longer needed in the coupled lateral standing-mode theory because of the $\sin(2\theta_K)$ factor already contained in $\Delta\omega_K$.

The critical-mode parameters shown in the upper part

of the figure also represent significant new results. The kink effect, manifested in the jump in the critical-mode θ_K value from close to 45° up to about 65° at $H \approx 1100$ Oe, is about the same as before. It is noteworthy that the θ_K values for low field are somewhat closer to the 45° value expected from the $\sin\theta_k \cos\theta_k$ coupling term in Eq. (2) that obtained previously in Refs. 6 and 13. The *ad hoc* $\sin^2(2\theta_k)$ term in the spin-wave linewidth used in Refs. 6 and 13 pushed the critical mode θ_K to lower values.

The important new result, however, is that the critical-mode K value no longer jumps to zero for static fields above the kink point. In the coupled lateral standing-mode theory, the critical-mode wave number now jumps to a value in the 5×10^4 cm^{-1} range for fields above the kink point. This is precisely the range of critical-mode K values found experimentally in the BLS experiments of Ref. 10. The theoretical basis for these large critical-mode K values is the inverse K dependence for the $\Delta\omega_K$ parameter already discussed.

In addition to the display of critical-mode K and θ_K values shown in Fig. 7, it is important to comment on the range of values for $\Delta\omega_K/\eta_k$ at these critical-mode points in the minimum threshold calculations. The sole justification for use of the Φ-independent G function in place of the Φ_k-dependent F functions for purposes of calculation was the end result of critical mode $\Delta\omega_K/\eta_k$ values below 1 or so. For the specific theoretical curves shown in Figs. 6 and 7, the numerical values of $\Delta\omega_K/\eta_k$ at the various critical-mode points ranged between 0.24 and 0.91. This means that the simplified threshold calculation based on the Φ_K-independent G function has the indicated empirical justification.

It is important to note, however, that the G-function approach was found to work well only if the large $\Delta\omega_K/\eta_k$ limit for G was set at fairly high values, such as the $(\pi/2)^2$ value used for Eq. (25). If substantially lower values were used, such as $\pi/2$, for example, problems were encountered in the minimization procedure due to the competition between the η_k factor in the numerator of Eq. (26) and the $1/\eta_k$ factor driving the $G(\Delta\omega_K/\eta_k)$ function. A better function, perhaps, would be to perform the 36×36 determinant analysis to determine the correct F value for each available $(\omega_K=\omega_p/2, K, \theta_K)$ state and do a rigorous minimum threshold determination based on these values. This procedure would be computationally tedious and complicated. Such an approach has not been attempted here.

Figure 8 provides a more detailed perspective on the K dependence of the thin-film critical-mode threshold microwave field amplitudes. The graphs show plots of $h_c^{\rm film}$ and $h_c^{\rm bulk}$ as a function of wave number K for the long configuration and two specific values of the static field H, 700 and 1300 Oe. All other parameters are the same as for the curves in Fig. 7. The top graph, for $H=700$ Oe, corresponds to the lower range of fields in the butterfly curve graph of Fig. 7 for which the critical-mode K value which minimizes $h_c^{\rm film}$ is large. The bottom graph, for $H=1300$ Oe, corresponds to the range of static fields above the kink point for which the critical-mode K value which minimizes $h_c^{\rm film}$ is small. Two curves are shown on each graph. The solid curves are from the coupled lateral mode theory. The dashed curves are from the bulk theory.

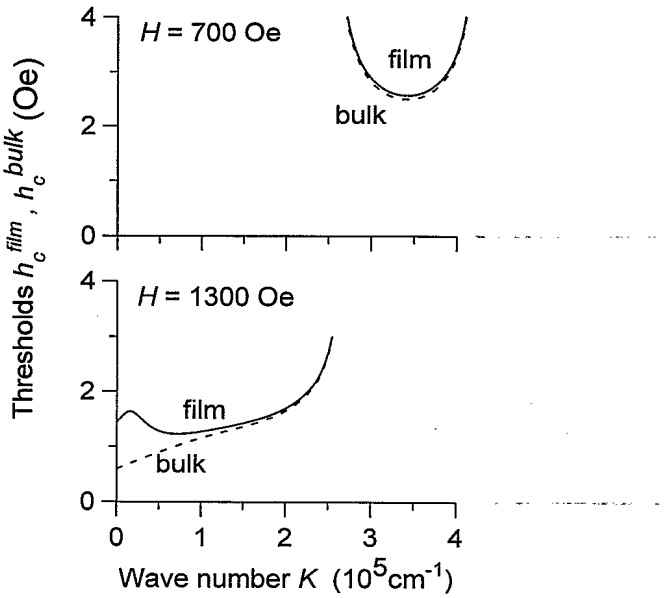

FIG. 8. Graphs of the calculated subsidiary absorption spin-wave-instability threshold microwave field amplitudes $h_c^{\rm film}$, from the coupled lateral mode thin-film theory, and $h_c^{\rm bulk}$, from the bulk limit theory, as a function of the operating point wave number K for the long configuration and two different values of the static in-plane magnetic field H, as indicated. The curves were obtained for the same parameters as used for Fig. 7. The solid lines are for $h_c^{\rm film}$ and the dashed lines are for $h_c^{\rm bulk}$.

Consider the upper graph in Fig. 8. Recall that at low field, the low wave-number part of the spin-wave band will be at low frequency, relative to the parametric spin waves at $\omega_p/2$. This means that the range of operating points at $\omega_K=\omega_p/2$ will be limited to relatively large K values, and to the full range of θ_K values from 90° to 0° as one moves from the minimum to the maximum of these allowed K values. These restrictions in K are evident in the limited range of K values, from about 2.5×10^5 to 4×10^5 cm^{-1}, for both of the curves in the top part of Fig. 8. The solid and dashed curves in the upper graph are very close to each other. This indicates that for this low field and relatively high critical-mode wave-number situation, the thin-film and bulk limit theories give about the same result. This is the result of the $1/K$ factor in $\Delta\omega_K$. When K is large, the $1/K$ factor pushes $\Delta\omega_K/\eta_k$ to small values and this, in turn, pushes the $G(\Delta\omega_K/\eta_k)$ to $G=1$. In this limit, the thin-film threshold in Eq. (26) reduces to the bulk limit threshold. The minimum threshold point from the top graph in Fig. 5 is at $K\approx3.5\times10^5$ cm^{-1}. This minimum threshold point is approximately midway between the lowest and the highest K values available at $H=700$ Oe. This point corresponds, therefore, to a spin-wave angle of about 45°. These values match the critical-mode K and θ_K parameters for $H=700$ Oe in Fig. 7.

Turn now to the lower graph in Fig. 8. Recall that at

high fields which correspond to the region above the kink point, the range of available K values at $\omega_K = \omega_p/2$ now starts at $K=0$ and extends up to some upper limit cutoff value which becomes smaller and smaller as H approaches the high-field butterfly-curve limit. For the parameters at hand, and at $H=1300$ Oe, this upper limit cutoff K value is about 2.5×10^5 cm^{-1}. The two curves in the bottom graph in Fig 8 extend over this $0-2.5\times10^5$ cm^{-1} range for K. Note that, as K increases from zero to its 2.5×10^5 cm^{-1} upper limit, θ_K is decreasing from some upper limit value at $K=0$ to zero.

The results in Fig. 8(b) show that when K is relatively large, above about 1×10^5 cm^{-1} or so, the calculated thresholds from the thin-film and bulk limit theories are about the same and the two curves are close together. This is the same as for the high-K situation in Fig. 8(a) discussed above. However, when K drops below about 1×10^5 cm^{-1}, the thin-film threshold h_c^{film} begins to increase, relative to bulk limit threshold h_c^{bulk}, goes through a relatively shallow minimum near $K=0.6\times10^5$ cm^{-1} or so, and then shows somewhat more complicated behavior for lower K values. It is clear from these results that the low K behavior of h_c^{film} is much more involved than that of h_c^{bulk}.

In order to understand the solid curve results in Fig. 8(b), it is necessary to realize that there are competing K dependences embedded in the h_c^{film} function of Eq. (26). The $1/K$ dependence for $\Delta\omega_K$ causes $G(\Delta\omega_K/\eta_k)$, and hence h_c^{film} as well, to increase as K decreases. The K dependence of ΔH_k, given through the Sparks' $L(k/k_c)$ function in Eq. (28), promotes a decrease in h_c^{film} with decreasing K when K is small. It is also important to remember that in order to maintain the spin-wave frequency operating point ω_K at $\omega_p/2$, any change in K must be accompanied by concurrent changes in θ_K. These changes in θ_K lead to further changes in $\Delta\omega_K$, and hence, to $G(\Delta\omega_K/\eta_k)$ and h_c^{film}, as K is changed. For the present experimental parameters, the net effect here is an upturn in h_c^{film} relative to the still decreasing h_c^{bulk} functional dependence for values of K below 1×10^5 cm^{-1} or so, the shallow minimum near $K=1\times10^5$ cm^{-1}, and then the more involved changes at even lower K. Keep in mind, as well, that all of the computations presented here are based on the G-curve approximation, rather than the actual Φ_K-dependent F functions from the coupled lateral mode analysis. A rigorous treatment would deal with the full F-function behavior and the θ_K dependences imbedded in Φ_K. Such an analysis is beyond the scope of this work.

Apart from the details of the dependences just discussed, the main point of Fig. 8 is in the demonstration of the coupled mode effects on the critical modes, that is, those modes with the minimum threshold, when the operational wave number K is small. The occurrence of the minimum threshold point at a nonzero K value derives from the $1/K$ dependence of a frequency spacing parameter for the array of coupled modes. Of even more importance from a general point of view, is that the effect is not limited to the thin-film geometry or the specific lateral coupled modes considered here. The basic results will apply equally to samples of any shape. The only requirement is to have some ensemble of standing spin-wave normal modes located close to the nominal spin-wave operating point. This requirement is satisfied, in particular, for sphere samples, the shape applicable to the initial experiments on fine structure by Jantz and Schneider[11,15] and on the kink effect by Patton and Jantz.[6] The present results provide the physical basis for the empirical determination by Jantz and Schneider that the operational critical modes in their experiments had rather large wave numbers, well above those expected for low-order magnetostatic modes. They also explain why various attempts to explain the shape of butterfly curves for static fields above the kink point on the basis of coupled low-order magnetostatic modes[16,17] were not successful.

The above results also relate to a recent model which attributes the relatively high wave-number critical modes for resonance saturation in YIG spheres to the influence of small micron size pits.[18] The results presented above show that the selection of critical modes at high K values stems directly from the frequency spacing of the standing modes in the sample and do not depend on special sources of scattering such as pits. The scaling of the F function with $1/K$ and $\sin(2\theta_K)$ should also be applicable to parallel pumping spin-wave-instability processes.

V. SUMMARY

This study has presented measurements of the subsidiary absorption spin-wave-instability threshold microwave field amplitude h_{crit} and corresponding butterfly curves of h_{crit} vs the in-plane static magnetic field H for yttrium iron garnet films of rectangular shape at 9.4 GHz. The microwave pumping field was also in-plane and perpendicular to the static field. The key new experimental result is in the measurement of different butterfly-curve profiles for different directions of the in-plane field. The expectation, based on theory to date, including thin-film theory, was that there should be no orientation dependence of the h_{crit} profiles.

The above statements notwithstanding, once one realizes that the various lateral standing magnetostatic modes across the film most be involved in the processes which determine the critical modes and the corresponding thresholds, it is reasonable to expect that orientation will affect the measured butterfly curves. Based on this realization, a recent theory for the first-order spin-wave-instability threshold in thin films was modified to take into account the coupling between the lateral standing modes across the film. The formal analysis, albeit complicated, yields a fairly simple procedure to take these coupled modes into account and compute butterfly curves and critical-mode parameters for comparison with experiment.

Butterfly curves and the corresponding critical-mode wave vectors were then calculated for YIG materials parameters, configurations which matched the experiments, and reasonable spin-wave linewidth parameters. The butterfly curves reproduced the basic features of the data. The critical modes were found to be about the same as

from the bulk limit theory for the low static field region of the subsidiary absorption butterfly curve, the region below the so-called kink point. In this region, the critical-mode wave numbers were large, in the $2-4\times10^5$ cm^{-1} range, and the critical-mode spin-wave angles were near 45°. This is the range of applicability expected for the bulk limit theory. For fields above the kink point, however, the critical-mode properties predicted from the coupled lateral mode theory are found to be quite different from the bulk limit theory. Here, the bulk limit theory predicts zero wave-number critical modes. The coupled lateral mode theory gives critical-mode wave numbers in the 5×10^4 cm^{-1} range. This is the same range of critical-mode wave numbers found experimentally by Brillouin light scattering. The above theoretical results were based on a wave-number-dependent spin-wave relaxation rate which is entirely consistent with known relaxation theory. In previous works, it was found necessary to introduce an *ad hoc* angle spin-wave angle-dependent term to fit the experimental data.

As a closing observation on the general problem of first order spin-wave-instability processes in magnetic systems, it is important to point out the general importance and relevance of the above results to samples other than magnetic thin films. The initial work which led to the realization of critical modes with wave numbers substantially greater than zero, cited as Ref. 11, was done for single-crystal YIG spheres. The initial discovery of the kink effect, cited as Ref. 6, was also for single-crystal YIG spheres. The general connection between the present thin-film results and the general problem lies in the properties of the frequency spacing parameter $\Delta\omega_K$ introduced in Sec. III B and given in approximate form in Eq. (17). The specific functional dependences of this parameter on spin-wave wave number and spin-wave angle were found to be precisely those which are needed (a) to achieve the good fits to the data noted above without recourse to *ad hoc* changes in the spin-wave linewidth, and (b) to obtain critical-mode wave number values in the 5×10^4 cm^{-1} range which match the results of the fine-structure measurements and the Brillouin light-scattering measurements noted above. Even though this analysis was done for the specific case of magnetic thin films, the basic K and θ_K dependences which are obtained are of a general nature.

ACKNOWLEDGMENTS

G.W. was supported in part by the Deutsche Forschungsgemeinschaft, Bonn, Germany. P.K. is on leave from the Faculty of Electrical Engineering and Information Technology, Slovak Technical University, Bratislava, Slovakia. The YIG films used in this work were kindly provided by Dr. J. D. Adam, Westinghouse Research Laboratories, Pittsburgh, Pennsylvania and Dr. P. DeGasperis, CNR, Rome, Italy. The research was supported in part by the United States Office of Naval Research, Grant Nos. N00014-90-J-4078 and N00014-94-1-0096, the National Science Foundation, Grant Nos. DMR-8921761 and DMR-9400276, and the United States Army Research Office, Grant No. DAAL03-91-G-0327.

APPENDIX

Consider a standing lateral mode located close to the $(\omega_K=\omega_p/2,K,\theta_K)$ and let the k_y and k_z wave-number components both change by $+\pi/L_y$ and $+\pi/L_z$, respectively. It is assumed, as in Sec. III, that $\pi/L_y \ll K$ and $\pi/L_z \ll K$ are satisfied. These small changes in k_y and k_z will result in changes in the lateral mode frequency as well, as specified by the $\Delta\omega_Y$ and $\Delta\omega_Z$ parameters defined through Eqs. (13) and (14) in Sec. III B. The overall frequency shift, $\delta\omega_k$, in terms of $\Delta\omega_Y$ and $\Delta\omega_Z$ is

$$\delta\omega_k=\Delta\omega_Y+\Delta\omega_Z \ . \tag{A1}$$

As pointed out in Sec. III B, $\Delta\omega_Y$ scales with π/L_y and $\Delta\omega_Z$ scales with π/L_z. It is this scaling which will allow the identification of specific functions for $\Delta\omega_Y$ and $\Delta\omega_Z$ at the end of this appendix. The polar frequency shift parameters $\Delta\omega_K$ and Φ_K were defined according to

$$\Delta\omega_Y=\Delta\omega_K\sin\Phi_K \tag{A2}$$

and

$$\Delta\omega_Z=\Delta\omega_K\cos\Phi_K \ . \tag{A3}$$

Expressions for $\Delta\omega_K$ and Φ_K as a function of $\Delta\omega_Y$ and $\Delta\omega_Z$ are given by Eqs. (15) and (16). Note that $\delta\omega_K$ may be positive or negative.

As an alternative to the above approach, one may also write the frequency shift $\delta\omega_k$ in terms of the changes in the wave number k and spin-wave propagation angle θ_k which accompany the above changes in k_y and k_z. From simple geometrical considerations in the $\pi/L_y \ll K$ and $\pi/L_z \ll K$ limits, these changes in k and θ_k may be written as

$$\Delta k=\frac{\pi}{L_y}\sin\theta_K+\frac{\pi}{L_z}\cos\theta_K \tag{A4}$$

and

$$\Delta\theta_k=\frac{1}{K}\left[\frac{\pi}{L_y}\cos\theta_K-\frac{\pi}{L_z}\sin\theta_K\right] . \tag{A5}$$

Recall that θ_k is the polar spin-wave propagation angle between the wave vector **K** and the z axis. Equations (A4) and (A5) follow directly from the geometry for a y-z plane wave vector **k** which is close to the operating point wave vector **K** at angle θ_K and undergoes y- and z-component increases by $+\pi/L_y$ and $+\pi/L_z$, respectively. The mode frequency shift $\delta\omega_k$ which accompanies these increases, expressed in terms of Δk and $\Delta\theta_k$, is given by

$$\delta\omega_k=\Delta k\frac{\partial\omega_k}{\partial k}\bigg|_{\omega_p/2,K,\theta_K}+\Delta\theta_k\frac{\partial\omega_k}{\partial\theta_k}\bigg|_{\omega_p/2,K,\theta_K} , \tag{A6}$$

where ω_k is the spin-wave frequency in the dispersion relation of Eq. (7), and the partial derivatives are evaluated at $\omega_k=\omega_K=\omega_p/2$, $k=K$, and $\theta_k=\theta_K$. These ω_k, k, and θ_k values correspond to the operating point already indicated.

It will prove convenient to define two functions of θ_K,

$A(\theta_K)$, and $B(\theta_K)$, given by

$$A(\theta_K)=K\frac{\partial\omega_k}{\partial k}\bigg|_{\omega_p/2,K,\theta_K} \tag{A7}$$

and

$$B(\theta_K)=\frac{\partial\omega_k}{\partial\theta_k}\bigg|_{\omega_p/2,K,\theta_K} . \tag{A8}$$

These functions may be evaluated explicitly from Eq. (7). The results of these evaluations are

$$A(\theta_K)=\frac{2[f(\theta_K)-\omega_H][2f(\theta_K)+\omega_m\sin^2\theta_K]}{\omega_p} \tag{A9}$$

and

$$B(\theta_K)=\frac{2f(\theta_K)\omega_m\sin\theta_K\cos\theta_K}{\omega_p} . \tag{A10}$$

The function $f(\theta_K)$ is given by

$$f(\theta_K)=\gamma(H+DK^2)$$
$$=\tfrac{1}{2}[\sqrt{(\omega_m\sin^2\theta_K)^2+\omega_p^2}-\omega_m\sin^2\theta_K] . \tag{A11}$$

Note that $f(\theta_K)$ is just the angle-dependent function which described the $\gamma(H+Dk^2)$ term in the dispersion, evaluated at the $(\omega_K=\omega_p/2,K,\theta_K)$ operating point.[8] Equations (A4)–(A11) may be combined to yield an expression for $\delta\omega_k$ in terms of K, θ_K, π/L_y, and π/L_z. The result is

$$\delta\omega_k=\frac{A(\theta_K)}{K}\left[\frac{\pi}{L_y}\sin\theta_K+\frac{\pi}{L_z}\cos\theta_K\right]$$
$$+\frac{B(\theta_K)}{K}\left[\frac{\pi}{L_y}\cos\theta_K-\frac{\pi}{L_z}\sin\theta_K\right] . \tag{A12}$$

Recall that $\delta\omega_k$ also has the form shown in Eq. (A1), and that terms in $\delta\omega_k$ with π/L_y or π/L_z factors will be associated with $\Delta\omega_Y$ or $\Delta\omega_Z$, respectively. The terms on the right-hand side of Eq. (A12) which contain π/L_y factors combine, therefore, to form $\Delta\omega_Y$. Those terms with π/L_z factors combine to form $\Delta\omega_Z$. In terms of a shorthand notation with $A(\theta_K)=A$, $B(\theta_K)=B$, $\sin\theta_K=S$, $\cos\theta_K=C$, one obtains

$$\Delta\omega_Y=(AS+BC)(\pi/L_y) \tag{A13}$$

and

$$\Delta\omega_Z=(AC-BS)(\pi/L_z) . \tag{A14}$$

These relations may then be combined according to Eq. (15) in Sec. III B to yield

$$\Delta\omega_K=\frac{1}{K}\sqrt{(AS+BC)^2(\pi/L_y)^2+(AC-BS)^2(\pi/L_z)^2} . \tag{A15}$$

One may also, if desired, obtain an explicit expression for Φ_K according to Eqs. (16), (A13), and (A14). The numerical results presented in Sec. VI were obtained on the basis of the expression for $\Delta\omega_K$ given by Eq. (A13).

Recall that the relatively simple expression for $\Delta\omega_K$ contained in Eq. (17) of Sec. III B was limited to cases for which the K dependence of ω_K could be neglected. From Eqs. (A4)–(A8), this corresponds to the condition $A(\theta_K)\ll B(\theta_K)$. In order to estimate the relative sizes of $A(\theta_K)$ and $B(\theta_K)$, consider the $A(\theta_K)/B(\theta_K)$ ratio obtained by dividing Eq. (A9) by Eq. (A10):

$$\frac{A(\theta_K)}{B(\theta_K)}=\frac{2[f(\theta_K)-\omega_H][2f(\theta_K)+\omega_m\sin^2\theta_K]}{2f(\theta_K)\omega_m\sin\theta_K\cos\theta_K} . \tag{A16}$$

Note that the first square bracket term in the numerator of Eq. (A16), $[f(\theta_K)-\omega_H]$, simply amounts to an effective exchange frequency given by γDK^2. Except for spin-wave angles close to $\theta_K=0°$ and $\theta_K=90°$, the magnitude of the $A(\theta_K)/B(\theta_K)$ ratio will on the order of $\gamma DK^2/\omega_m$, or equivalently, $DK^2/4\pi M_s$. For the range of K values of importance here, in the range 10^4–10^5 cm^{-1} or so, and with a YIG spin-wave stiffness constant D of 5.4×10^{-9} Oe cm^2 and saturation induction $4\pi M_s$ of 1750 G, this $DK^2/4\pi M_s$ ratio is in the 10^{-3}–10^{-4} range. This means that for the midrange of θ_K values which are typically involved in subsidiary absorption, $A(\theta_K)$ will be much smaller than $B(\theta_K)$ and may be ignored. If these A terms in Eq. (A16) are deleted, one obtains the $\Delta\omega_K$ expression given by Eq. (17).

[1]H. Suhl, J. Phys. Chem. Solids **1**, 209 (1957).
[2]R. W. Damon, in *Magnetism,* edited by G. T. Rado and H. Suhl (Academic, New York, 1963), Vol. 1.
[3]N. Bloembergen and R. W. Damon, Phys. Rev. **93**, 72 (1954).
[4]E. Schlömann, J. Phys. Soc. Jpn. **17**, Suppl. B-I, 406 (1961).
[5]C. E. Patton, in *Magnetic Oxides,* edited by D. J. Craik (Wiley, London, 1975), pp. 575–645.
[6]C. E. Patton and W. Jantz, J. Appl. Phys. **50**, 7082 (1979).
[7]E. Schlömann, Raytheon Company, Technical Report R-48, 1959.
[8]C. E. Patton, J. Appl. Phys. **40**, 2837 (1969).
[9]M. Chen and C. E. Patton, in *Nonlinear Phenomena and Chaos in Magnetic Materials,* edited by P. E. Wigen (World Scientific, Singapore, 1994), pp. 33–82.
[10]W. D. Wilber, J. G. Booth, C. E. Patton, G. Srinivasan, and R. W. Cross, J. Appl. Phys. **64**, 5477 (1988).
[11]W. Jantz and J. Schneider, Phys. Status Solidi A **31**, 595 (1975).
[12]G. Wiese, Z. Phys. B **91**, 57 (1993).
[13]G. Wiese, P. Kabos, and C. E. Patton, J. Appl. Phys. **74**, 1218 (1993).
[14]M. Sparks, *Ferromagnetic Relaxation Theory* (McGraw-Hill, New York, 1964).
[15]W. Jantz and J. Schneider, Solid State Commun. **10**, 937 (1972).
[16]P. H. Bryant, Phys. Rev. B **39**, 4363 (1989).
[17]M. Chen and C. E. Patton, J. Appl. Phys. **69**, 5724 (1991).
[18]H. A. Krug von Nidda, G. Wiese, and H. Benner, Z. Phys. B **95**, 55 (1994).